TAMPEREEN TEKNILLINEN YLIOPISTO
TAMPERE UNIVERSITY OF TECHNOLOGY

LIISA NASKALI

INTEGRATION AND SYNCHRONIZATION OF DEVICES IN A NONLINEAR MICROSCOPY SETUP

Master of Science Thesis

Examiners: **Prof. Martti Kauranen and Dr. Godofredo Bautista**
Examiners and topic approved by the Council of the Faculty of Natural Sciences on December 3, 2014

ABSTRACT

TAMPERE UNIVERSITY OF TECHNOLOGY
Master's Degree Programme in Science and Engineering
NASKALI, LIISA: Integration and synchronization of devices in a nonlinear microscopy setup
Master of Science Thesis, 65 pages, 3 Appendix pages
March 2015
Major: Advanced Engineering Physics
Examiners: Prof. Martti Kauranen and Dr. Godofredo Bautista
Keywords: Nonlinear optics, microscopy, second-harmonic generation, third-harmonic generation, LabVIEW

Nonlinear microscopy is used for investigating a variety of biological systems and artificial materials. The contrast achieved in this imaging technique relies on the detected signals that arise from nonlinear interactions between a pulsed excitation beam and the specimen. As these nonlinear interactions are spatially localized, i.e., the signal originates only from a small focal volume, this technique permits intrinsic three-dimensional imaging. In order to acquire an image, either beam scanning with a fixed sample or sample scanning with respect to a fixed beam is used.

In this Thesis, we developed and tested the performance of a home-built point-scanning nonlinear microscope. In the development, it is critical to integrate and synchronize the components of a nonlinear microscope. For example, as the excitation beam is focused and thus the spot covers only a very small area in the sample, a scanning stage is needed that is computer-controlled and synchronized with photodetectors that measure the intensity of the nonlinear signal. If the polarization of the excitation beam needs to be carefully defined and changed between measurements, a motorized wave plate also needs to be computer-controlled. Here, the controls of the scanning stage, detectors and the wave plate were integrated into a single program, and a functional user interface in the LabVIEW environment was developed. The program enables the adjustment of the measurement parameters, monitoring of the measurements and saving of the results. Furthermore, the program was modified so that additional devices can be integrated into it in the future, and thus the microscopy setup is not restricted only to the kinds of measurements shown in this Thesis.

The performance of the developed program was tested using artificial nano-sized gold particles. The microscopy setup and the controlling program were found to work properly and reliably, and the detected signals were confirmed to originate from second- and third-harmonic phenomena in which the output signal has a frequency of two or three times the original one, respectively. As expected for the second-harmonic response, samples with chiral properties had different responses for the two opposite circular polarizations. Additionally, we found that the third-harmonic response also exhibits different but weak responses under circular polarizations. Our results suggest the great potential of nonlinear microscopy for studying nonlinear circular dichroism effects in artificial nanomaterials.

TIIVISTELMÄ

TAMPEREEN TEKNILLINEN YLIOPISTO
Teknis-luonnontieteellinen koulutusohjelma
NASKALI, LIISA: Laitteiden synkronointi ja integrointi epälineaarisessa mikroskoopissa
Diplomityö, 65 sivua, 3 liitesivua
Maaliskuu 2015
Pääaine: Teknillinen fysiikka
Tarkastajat: professori Martti Kauranen ja tohtori Godofredo Bautista
Avainsanat: Epälineaarinen optiikka, mikroskopia, taajuudenkahdennus, taajuudenkolmennus, LabVIEW

Epälineaarista mikroskopiaa, jossa mitattava signaali syntyy fokusoidun pulssitoimisen lasersäteen ja näytteen välisessä epälineaarisessa vuorovaikutuksessa, käytetään sekä biologisten systeemien että synteettisten materiaalien tutkimuksessa. Epälineaarisissa prosesseissa vaste on peräisin hyvin pienestä näytetilavuudesta, mikä mahdollistaa kolmiulotteisen kuvantamisen. Koska epälineaarisessa mikroskoopissa käytetään fokusoitua lasersädettä, näytettä täytyy liikuttaa mittauksen aikana suhteessa säteeseen tai päinvastoin.

Tässä diplomityössä kehitettiin ja testattiin käyttöliittymä itse rakennettuun epälineaariseen mikroskooppiin. Käyttöliittymää toteutettaessa on tärkeää ottaa huomioon, että siihen liitettyjen laitteiden, kuten näytteensiirtoalustan ja epälineaarisia signaaleja mittaavien fotoni-ilmaisimien, tulee toimia oikea-aikaisesti suhteessa toisiinsa. Myös herätekentän polarisaatiotilan muuttamiseen käytettävän polarisaattorin ohjaus voidaan yhdistää samaan ohjelmaan näytealustan ja ilmaisimien kanssa, kuten tässä työssä tehtiin.

LabVIEW-ympäristössä luodun ohjelman avulla voidaan säätää mittausparametreja, tarkkailla mittauksen etenemistä ja tallentaa tulokset. Ohjelma toteutettiin siten, että uusien ominaisuuksien ja laitteiden lisääminen siihen on mahdollista myöhemminkin, koska kyseistä mikroskooppia saatetaan tulevaisuudessa käyttää myös muunlaisiin mittauksiin kuin mihin tässä työssä on keskitytty.

Toteutetun ohjelman toimintaa tutkittiin mittaamalla kullasta valmistettujen nanokokoluokan näytteiden epälineaarisia vasteita. Mikroskooppi ja kehitetty ohjelmisto todettiin toimiviksi, luotettaviksi sekä helppokäyttöisiksi. Mittauksissa varmistettiin, että epälineaariset signaalit aiheutuvat taajuudenkahdennuksesta ja -kolmennuksesta, jolloin syntyvän säteilyn taajuus on kaksin- tai kolminkertainen alkuperäisen herätekentän taajuuteen nähden riippuen kummasta ilmiöstä on kysymys. Taajuudenkahdennuksen tapauksessa kiraalisten näytteiden vaste oli oletetusti erilainen oikea- ja vasenkätisesti ympyräpolarisoiduille herätekentille. Lisäksi huomasimme, että myös taajuudenkolmennuksen tapauksessa havaitaan sama ilmiö, joskin heikkona. Tämä antaa viitteitä siitä, että tulevaisuudessa kyseisen kaltaisia näytteitä voidaan tutkia epälineaaristen vasteiden avulla.

PREFACE

This Master's Thesis project was carried out in the Optics Laboratory of the Department of Physics at Tampere University of Technology (TUT). The starting point of the project was interesting, practical, and challenging. There was a new nonlinear optical microscope soon to arrive in the laboratory, but the user interface for the scanning and detection system of the microscope was missing. My task was to implement the interface in the LabVIEW environment.

I thank Prof. Martti Kauranen for trusting in my ability to manage the project. I have now worked in the Optics Laboratory for two and a half years, but before this Master's Thesis project my main expertise was programming with MATLAB and working with numbers and graphs. This project has thus offered me plenty of experience on working in a laboratory, practise in microscopy, and handling laser beams. It has also been very interesting to study a new programming language and to get myself involved with programming many devices in order to integrate them to work together.

Besides the important help and support of Prof. Kauranen, I also want to thank my other examiner and supervisor Dr. Godofredo Bautista for the support, help and patience he has offered to me during this project and also before it. The measurements analysed in Chapter 6 were made in collaboration with Dr. Bautista and Mr. Léo Turquet, and the samples investigated were fabricated by Dr. Israel De Leon (University of Ottawa, Canada). The Master's Thesis of Timo Lehto, entitled "Epälineaarisen optisen mikroskoopin rakentaminen", from the year 2009 has offered a lot of support to this project, too, as it deals with the same subject as my Thesis. In addition, my great acknowledgements goes to my former supervisor Dr. Mikko J. Huttunen, who has still engaged into fruitful discussions and had patience to answer my questions during this year even if we are not working in the same laboratory anymore.

As my over six-year path at TUT and almost three-year-path in Optics is almost over, it is time to thank many other people, too. Elisa, Mari and Jan: it was a great pleasure to share a room with you and being friends also outside the work. Special thanks to Elisa for sharing not only the room, but also all these years at TUT, since our first day here! The whole Optics Laboratory also deserves applause for making the spirit in the Laboratory so fantastic. Finally, thanks to my parents for supporting me both physically and mentally during my student years, and to Tuomo, especially for scientific peer support and proofreading during this Thesis project.

Tampere 17.2.2015

Liisa Naskali

TABLE OF CONTENTS

SYMBOLS AND ABBREVIATIONS

We use tilde (~) for time-varying quantities. **Bold** (*italic*) font is used for vector (scalar) quantities.

Symbols

A	absorbance
$\tilde{\boldsymbol{B}}$	magnetic induction
c	speed of light in vacuum
c.c.	complex conjugate
*	complex conjugate
$\tilde{\boldsymbol{D}}$	electric displacement
$\tilde{\boldsymbol{E}}$	electric field
E_0	amplitude of electric field
$\tilde{\boldsymbol{H}}$	magnetic field
i	imaginary unit
I	intensity
$\hat{\boldsymbol{i}}, \hat{\boldsymbol{j}}$	unit vectors
$\tilde{\boldsymbol{J}}$	electric current density
k	wave number
$\tilde{\boldsymbol{M}}$	magnetization
n	refractive index
$\tilde{\boldsymbol{P}}$	electric polarization
P	power
$\boldsymbol{r}$	position vector
t	time
v	speed of wave
x, y, z	Cartesian coordinates
ε	permittivity of material
ε_0	permittivity of vacuum
ε_r	relative permittivity
λ	wavelength
μ	permeability of material
μ_0	permeability of vacuum
μ_r	relative permeability
ν	frequency
$\tilde{\rho}$	electric charge density
$\Delta\phi$	phase difference

$\chi^{(n)}$	susceptibility of n^{th} order
ψ	wave function
ω	angular frequency

Abbreviations

3D	three-dimensional
CD	circular dichroism
CMOS	complementary metal oxide semiconductor
CPM	chiral plasmonic metamaterial
CW	continuous-wave
DFG	difference-frequency generation
DLL	dynamic-link library
FWHM	full width at half maximum
FWM	four-wave mixing
HWP	half-wave plate
LH	left-handed
LHCP	left-handed circular polarization
MRU	miniature recirculating unit
NLO	nonlinear optical
NLOM	nonlinear optical microscopy
OR	optical rectification
PBS	polarizing beam splitter
PMT	photomultiplier tube
QWP	quarter-wave plate
RH	right-handed
RHCP	right-handed circular polarization
SEM	scanning electron micrograph
SFG	sum-frequency generation
SHG	second-harmonic generation
SI	Systéme international d'unités, International System of Units
SPEF	single-photon excited fluorescence
THG	third-harmonic generation
TPEF	two-photon excited fluorescence
TUT	Tampere University of Technology

1. INTRODUCTION

Light is a prerequisite for human life as photosynthesis forms the basis for food production. Thus, mankind has always utilized sunlight, even though deeper understanding about what light is and how it behaves, has only been known for a few centuries. Nowadays, light is also important from a technological point of view. Actually, the United Nations declared 2015, this year, as the International Year of Light and Light-Based Technologies to highlight the importance of light and improve our understanding of light-based technologies in our everyday life and how they can be utilized even more in the future. For instance, everyone knows that we cannot see anything without light, but light can also help us in the fields of energy production, education, agriculture, communications and health, as some examples. [1]

The field of studying light and its interaction with matter is called optics. As seeing is very closely related to our lives, it is not surprising that light has interested people for a very long time. The first optical devices, mirrors, were made over 3000 years ago [2]. Nowadays, when the most popular hobby seems to be taking selfies, it is quite an odd thought that before mirrors the only way you could see your own face was from a surface of liquid. Also a positive lens, which focuses light, was known at least over 2000 years ago [2]. Beginning from mirrors and lenses, the development of optics, both its theory and practical applications, has given many helpful tools for the mankind during the centuries. For example, an invention of spectacles is dated to the 13th century and some kinds of monocles have probably existed even before that. In the end of the 16th century, it was realized that when multiple lenses are combined, even better magnification can be achieved compared to one magnifying lens. The resulting device, a microscope, is used to distinguish very small objects or details, structures and mechanisms. Shortly after the microscope, the inverse device for it, a telescope, was invented by Galileo in the beginning of 17th century enabling the observation of objects that are far away. [3] Thus, the principles of many optical devices are old, but of course their quality and properties have improved a lot during time, hand-in-hand with new knowledge, skills, and demands.

The starting point to the huge development of optics and optical devices in the 20th century was the invention of the quantum nature of the light. Based on that, the first laser was built up in the 1960s, providing a new kind of light source producing a high-power coherent beam. Hence, a new era in optics started and led to the discoveries of many novel phenomena and the invention of devices and applications. [2] Today, lasers are almost everywhere. In our everyday life we use lasers and related technologies, for example, in CD players, scanning labels in supermarkets and laser pointers in seminars.

In industry, lasers are used in many machines, for instance, for alignment and cutting or welding steel. In hospitals, lasers are offering new methods for both research and treatment activities. Lasers also transformed how people communicate as evidenced by laser-based fiber optics which enables fast communication and transfer of huge amounts of data quickly over long distances.

One of the new and significant optical fields discovered after the invention of the laser was nonlinear optics [4]. Usually, the nonlinear effects are so weak that we cannot detect them, but with intense laser light they become observable. In this Thesis, the focus is on two nonlinear effects called second- (SHG) and third-harmonic generation (THG), and especially their use in microscopy. In these phenomena, the strong excitation field interacts with a material in a way that produces new frequency components. In SHG, the frequency is doubled and, in THG, it is tripled compared to the frequency of the original field.

In nonlinear microscopy, the excitation field is focused to the sample and the magnified image is formed by detecting point-by-point the nonlinear signal coming from the sample. The nature of the nonlinear phenomena enables three-dimensional (3D) measurements as the signal always originates only from a small focal volume. The applications of SHG and THG microscopy include, among others, the study of surface effects, investigation of collagen or lipid ordering in tissues and cells and research of nanostructures. [5-7] In the future, these methods have been predicted to have a significant role in, for instance, biomedical applications. In this Thesis, SHG and THG microscopy are used to characterize artificial nano-sized materials.

The nonlinear microscope, in general, consists of a pulsed laser source with a pulse width on the femtosecond scale, a microscope objective, a beam or sample scanning instrument and a detector. If the microscope is used for polarized microscopy, meaning that the polarization state of the input light is changed during the measurements, a polarizer is also included in the setup. The aim of this Thesis was to integrate and synchronize the main components of a nonlinear microscope, i.e., to create and develop a program and a user interface for controlling these devices. The demand for this microscopy system was initiated when a new ultrafast laser was granted to the Optics Laboratory in Tampere University of Technology to advance nonlinear microscopy research.

The microscope is designed to be used for a variety of unique applications. This is why the program has to be developed in such a way that it would be as easy to use as possible. It is also foreseen that new devices and features need to be included in the setup later. The actual implementation of the program was made by a graphical programming language called LabVIEW. The devices included in the program were a polarizer, a scanning stage used for moving the sample in relation to the input laser beam, and two photomultiplier tubes (PMTs) used as the detectors for nonlinear signals.

The Thesis is divided into 7 chapters. After this Introduction, the basic theory of optics and the fundamentals of linear and nonlinear optics are described in Chapter 2. This includes the introduction of the SHG and THG phenomena, as the testing of the microscope is implemented by doing SHG and THG microscopy. The principles behind non-

linear optical microscopy are discussed in Chapter 3 including the difference between linear and nonlinear microscopy. Some applications are mentioned along with the meaning of polarized microscopy highlighted with the introduction of circular dichroism phenomena at the end of the chapter. The description of the microscopy setup and the features of the program are explained in Chapters 4 and 5. Chapter 6 describes the results achieved when testing the operation of the microscope and especially its control program. The samples used were plasmonic metamaterials, generally discussed in Chapter 3, and more closely introduced in the beginning of Chapter 6. In Chapter 7, the main parts of this Thesis are concluded.

2. OPTICS

2.1 The nature of light

Optics is the sub-area of physics that encompasses all studies about light, its properties and its interactions with matter. As human vision is based on light interacting with objects and our eyes, the mystery of light has sparked interest and investigated for millennia. Even the written history of optics is more than 2000 years old, as the Greek mathematician Euclid wrote his work *Optics* at around 300 B.C. The principles he proposed, for example that light would only be associated with human vision, are, however, now mostly known to be wrong. Nevertheless, there is at least one principle we agree on even today: *in homogenous media, light travels in straight lines*. [8]

After the Greeks, the study of optics had a low profile in Europe for more than a millennium. In the East, however, progressive ideas of light and its properties were developed. For example, the ideas of the finite speed of light and light as a stream of particles were proposed at around the year 1000. [8] Further development of the theory of optics was seen in the 17th century, when European physicists presented some optical theories with many different and even contradictory properties. One common property of light, however, showed up in many of them: *light consists of particles*. [2,8]

On the other hand, the early theories on the wave properties of light were also proposed in the 17th century. In the beginning of the 19th century, more experiments supporting the wave theory were made and finally the wave theory of light was accepted after James Clerk Maxwell (1831-1879) had presented his electromagnetic wave equations. [2,8,9] The development of quantum optics in the 20th century again raised the question of the particle nature of light, and nowadays light is described in terms of wave-particle duality [2].

Wave-particle duality means that, depending on the phenomenon, light can be treated as particles or as a wave. In this Thesis, both wave and particle natures of light are needed. When a laser beam propagates along the microscopy setup, we are interested in the shape of the beam and its polarization, both of which are closely related to the wave theory. These phenomena are described in this Chapter. Finally, when light from an imaged object is measured, the detected quantity is photons, meaning individual light particles. However, the theory of the particle nature of light is excluded from this Thesis.

2.2 Maxwell's equations and wave equation

In the 19th century, Maxwell extended the knowledge of the connection between light and electromagnetism by theoretically predicting the speed of light based on his electromagnetic studies [2,9]. Maxwell's equations describe the propagation of an electromagnetic wave, which consists of electric ($\tilde{\boldsymbol{E}}$) and magnetic ($\tilde{\boldsymbol{H}}$) components, in any medium. These four equations, in SI (Systéme international d'unités, International System of Units) units, are [10,11]

$$\nabla \cdot \tilde{\boldsymbol{D}} = \tilde{\rho}\,, \tag{2.1}$$

$$\nabla \cdot \tilde{\boldsymbol{B}} = 0\,, \tag{2.2}$$

$$\nabla \times \tilde{\boldsymbol{E}} = -\frac{\partial \tilde{\boldsymbol{B}}}{\partial t}, \tag{2.3}$$

$$\nabla \times \tilde{\boldsymbol{H}} = \frac{\partial \tilde{\boldsymbol{D}}}{\partial t} + \tilde{\boldsymbol{J}}\,. \tag{2.4}$$

The vector $\tilde{\boldsymbol{D}}$ is called electric displacement, $\tilde{\boldsymbol{B}}$ magnetic induction, $\tilde{\boldsymbol{J}}$ free electric current density, $\tilde{\rho}$ free electric charge density, and t means time. The tilde is used to refer to a quantity varying rapidly in time, e.g., oscillating at optical frequencies. We are interested in materials without free charges and free currents, so that [10,11]

$$\tilde{\rho} = 0 \tag{2.5}$$

and

$$\tilde{\boldsymbol{J}} = 0\,. \tag{2.6}$$

The relation between the electric field vector and the electric displacement is

$$\tilde{\boldsymbol{D}} = \varepsilon_0 \tilde{\boldsymbol{E}} + \tilde{\boldsymbol{P}}\,, \tag{2.7}$$

where ε_0 is the permittivity of vacuum and $\tilde{\boldsymbol{P}}$ the electric polarization, i.e., the response of a material to an optical field. The magnetic field vector and magnetic induction are related to each other in a similar way

$$\tilde{\boldsymbol{B}} = \mu_0 \tilde{\boldsymbol{H}} + \tilde{\boldsymbol{M}}\,, \tag{2.8}$$

where μ_0 is the permeability of vacuum and $\tilde{\boldsymbol{M}}$ is the magnetization [11]. In the cases of our interest, the material can be assumed to be nonmagnetic so that [10]

$$\tilde{\boldsymbol{M}} = 0 \tag{2.9}$$

and thus Eq. (2.8) reduces to the form

$$\tilde{\boldsymbol{B}} = \mu_0 \tilde{\boldsymbol{H}} \ . \tag{2.10}$$

When taking the curl of Eq. (2.3), by changing the order of the curl and the time derivative in the right hand side of the equations, and by inserting Eq. (2.10) into Eq. (2.3), we obtain

$$\nabla \times \nabla \times \tilde{\boldsymbol{E}} = -\frac{\partial}{\partial t}\left(\nabla \times \tilde{\boldsymbol{B}}\right) = -\frac{\partial}{\partial t}\left(\nabla \times \left(\mu_0 \tilde{\boldsymbol{H}}\right)\right). \tag{2.11}$$

Now we can utilize Eqs. (2.4) and (2.6) and obtain

$$\nabla \times \nabla \times \tilde{\boldsymbol{E}} = -\mu_0 \frac{\partial}{\partial t}\left(\nabla \times \tilde{\boldsymbol{H}}\right) = -\mu_0 \frac{\partial^2}{\partial t^2} \tilde{\boldsymbol{D}} . \tag{2.12}$$

Furthermore, we can insert Eq. (2.7) into this equation, thus producing the relation

$$\nabla \times \nabla \times \tilde{\boldsymbol{E}} = -\mu_0 \frac{\partial^2}{\partial t^2}\left(\varepsilon_0 \tilde{\boldsymbol{E}} + \tilde{\boldsymbol{P}}\right) = -\mu_0 \varepsilon_0 \frac{\partial^2}{\partial t^2} \tilde{\boldsymbol{E}} - \mu_0 \frac{\partial^2}{\partial t^2} \tilde{\boldsymbol{P}} . \tag{2.13}$$

By rearranging, we obtain the equation

$$\nabla \times \nabla \times \tilde{\boldsymbol{E}} + \mu_0 \varepsilon_0 \frac{\partial^2}{\partial t^2} \tilde{\boldsymbol{E}} = -\mu_0 \frac{\partial^2}{\partial t^2} \tilde{\boldsymbol{P}} . \tag{2.14}$$

Eq. (2.14) is a very general form of the optical wave equation describing the propagation of an optical wave in a medium [10]. The implication of Eq. (2.14) is discussed in more detail in Sections 2.3 and 2.4 for linear and nonlinear cases, respectively. It can be shown that when either the electric or the magnetic field of an electromagnetic wave is known, it can be used to completely specify the other field and thus the whole wave [9]. In this Thesis, we only use electric fields to describe the electromagnetic waves.

2.3 Linear optics

The material polarization $\tilde{\boldsymbol{P}}$ is defined as a dipole moment per unit volume. In the case of linear optics, the polarization is

$$\tilde{\boldsymbol{P}} = \tilde{\boldsymbol{P}}^{(1)} = \varepsilon_0 \boldsymbol{\chi}^{(1)} \tilde{\boldsymbol{E}} , \tag{2.15}$$

where $\chi^{(1)}$ is a linear, or first-order, optical susceptibility [10]. The term linear polarization is used because of the fact, that, as can be seen from Eq. (2.15), the first-order polarization is linearly proportional to the electric field inducing it. However, let's first concentrate on the situation in vacuum, where susceptibility equals to zero. Then, Eq. (2.14) turns to the form of

$$\nabla \times \nabla \times \tilde{\boldsymbol{E}} + \mu_0 \varepsilon_0 \frac{\partial^2}{\partial t^2} \tilde{\boldsymbol{E}} = 0 . \tag{2.16}$$

This can be furthermore simplified by using the vector identity

$$\nabla \times \nabla \times \tilde{\boldsymbol{E}} = \nabla\left(\nabla \cdot \tilde{\boldsymbol{E}}\right) - \nabla^2 \tilde{\boldsymbol{E}} , \tag{2.17}$$

and the fact that, in the cases we are interested in, the divergence of the electric field is negligible [10]

$$\nabla \cdot \tilde{\boldsymbol{E}} \approx 0 . \tag{2.18}$$

Thus, Eq. (2.16) can be expressed as

$$\nabla^2 \tilde{\boldsymbol{E}} - \mu_0 \varepsilon_0 \frac{\partial^2}{\partial t^2} \tilde{\boldsymbol{E}} = 0 . \tag{2.19}$$

It is worth noting that Eq. (2.19) has the form of a homogenous wave equation

$$\nabla^2 \psi - \frac{1}{v^2} \frac{\partial^2}{\partial t^2} \psi = 0 \tag{2.20}$$

which describes a wave with velocity *v* [2]. Hence, the speed of an optical wave in vacuum, marked as *c*, is

$$c = \frac{1}{\sqrt{\mu_0 \varepsilon_0}} . \tag{2.21}$$

One solution to the wave equation is a plane wave. In the one-dimensional case the equation describing an electromagnetic plane wave propagating to the positive *z*-direction is

$$E(z,t) = E e^{i(kz - \omega t)} \tag{2.22}$$

where *i* is imaginary unit, *k* is a wave number and ω is an angular frequency. The angular frequency is defined in terms of frequency ν of the field as [12]

$$\omega = 2\pi\nu \,. \tag{2.23}$$

In this Thesis, we refer to angular frequency as frequency as these two quantities are trivially proportional to each other. There is no chance for confusion as no numerical values for the frequencies are used. Instead, exact values are used for wavelength, which is related to frequency as

$$\lambda = \frac{c}{\nu} = \frac{2\pi c}{\omega}. \tag{2.24}$$

The wavelength and frequency are thus inversely proportional to each other. The wave number *k*, also known as a propagation constant, is defined as [12]

$$k = \frac{2\pi}{\lambda} = \frac{\omega}{c}. \tag{2.25}$$

Let's next study the case where the wave is not anymore in vacuum, but instead it propagates through an isotropic medium which has non-zero first-order susceptibility. Here, isotropy means that the propagation direction of the light in the material can be arbitrary without changing the interaction properties between light and the material. Thus, by combining Eqs. (2.14) and (2.15) and using the methods mentioned above, we obtain the following form of the wave-equation

$$\nabla^2 \tilde{\boldsymbol{E}} - \frac{1+\boldsymbol{\chi}^{(1)}}{c^2}\frac{\partial^2}{\partial t^2}\tilde{\boldsymbol{E}} = 0 \tag{2.26}$$

which describes a wave propagating with speed

$$v = \frac{c}{\sqrt{1+\boldsymbol{\chi}^{(1)}}}, \tag{2.27}$$

which is not equal to the speed of light in vacuum. On the other hand, similar to Eq. (2.21), the speed of the wave can be defined as

$$v = \frac{1}{\sqrt{\mu\varepsilon}} = \frac{1}{\sqrt{\mu_r\mu_0\varepsilon_r\varepsilon_0}}, \tag{2.28}$$

where μ_r and ε_r are the relative permeability and permittivity, respectively, of the medium [2]. In the cases we are interested in, the relative permeability is almost one, and thus the permeability of the material equals to the permeability of the vacuum. By combining the previous fact and Eqs. (2.21), (2.27) and (2.28) we find that the relation between the relative permittivity and the susceptibility is

$$\varepsilon_r = 1 + \chi^{(1)}. \tag{2.29}$$

The ratio of the speed of an electromagnetic wave in vacuum to that in matter is defined as the index of refraction, or refractive index *n* [2]. From Eq. (2.27) we can derive that in our case it is

$$n \equiv \frac{c}{v} = \sqrt{1 + \chi^{(1)}} = \sqrt{\varepsilon_r}\,. \tag{2.30}$$

For homogenous, isotropic media the refractive index is constant regardless of the propagation direction of the wave. However, this is not always the case, because some materials are optically anisotropic. For example, a material showing two different refractive indices for perpendicular directions is said to be birefringent. [2] Birefringence is considered more closely in Section 2.8.

2.4 Introduction to nonlinear optics

In Section 2.3, we concentrated on the linear wave equation for vacuum and then for an isotropic medium. However, in general, the polarization can be expressed as a sum of linear and nonlinear polarizations

$$\tilde{\boldsymbol{P}} = \tilde{\boldsymbol{P}}^{(1)} + \tilde{\boldsymbol{P}}^{(\mathrm{NL})} = \tilde{\boldsymbol{P}}^{(1)} + \tilde{\boldsymbol{P}}^{(2)} + \tilde{\boldsymbol{P}}^{(3)} + \ldots, \tag{2.31}$$

where $\tilde{\boldsymbol{P}}^{(2)}$ and $\tilde{\boldsymbol{P}}^{(3)}$ are the second- and the third-order polarizations, respectively. In the cases we are interested in, the polarization depends on the electric field according to the equation

$$\tilde{\boldsymbol{P}} = \varepsilon_0 \chi^{(1)} \tilde{\boldsymbol{E}} + \varepsilon_0 \chi^{(2)} \tilde{\boldsymbol{E}}^2 + \varepsilon_0 \chi^{(3)} \tilde{\boldsymbol{E}}^3 + \ldots \tag{2.32}$$

where $\chi^{(2)}$ and $\chi^{(3)}$ are the second- and third-order nonlinear optical (NLO) susceptibilities, respectively. The term linear refers to the first-order term and the higher-order terms are the nonlinear ones. This division is used as in linear optics only the first term is relevant and the others are related to nonlinear phenomena.

The susceptibilities are tensors. For example, the second-order susceptibility is a third-rank tensor with 27 components and the third-order susceptibility is a fourth-rank

tensor with 81 components. The susceptibility tensors are specific to each material and in general the values of the susceptibility components are complex numbers [10]. However, they are often approximated as real numbers. Sometimes, this is a good approximation, but some physical properties of the materials can only be understood through complex-valued susceptibilities [13]. A prominent example is the absorption of light, which arises from the imaginary part of the linear susceptibility. In addition, circular dichroism, explained in more detail in Section 2.9, is an effect which requires treatment with a complex-valued susceptibility. [14]

As discussed in Section 2.3, in linear optics only the first term in Eq. (2.32) is taken into account. In everyday life, only linear optical effects play a role, as the nonlinear effects are usually very weak. However, the nonlinear polarization is not linearly proportional to the electric field, but the relation is proportional to the higher powers of electric field as can be seen from Eq. (2.32). Thus, when using intense optical fields, the nonlinear terms can become significant, because they grow relatively more than the linear term for growing field strength. Sufficiently strong optical fields for making nonlinear effects observable can be created, for example, by lasers. [4,10]

In Section 2.2, we derived the general wave equation. When it is combined with Eq. (2.32), the origin of NLO effects can be seen. As was shown in Section 2.3, the first term of Eq. (2.14) can be simplified a bit and thus we can take the general wave equation as

$$\nabla^2 \tilde{\boldsymbol{E}} - \frac{1}{c^2}\frac{\partial^2}{\partial t^2}\tilde{\boldsymbol{E}} = \frac{1}{\varepsilon_0 c^2}\frac{\partial^2}{\partial t^2}\tilde{\boldsymbol{P}} \,. \tag{2.33}$$

When inserting Eq. (2.32) in the form

$$\tilde{\boldsymbol{P}} = \varepsilon_0 \, \boldsymbol{\chi}^{(1)} \tilde{\boldsymbol{E}} + \tilde{\boldsymbol{P}}^{(\mathrm{NL})} \tag{2.34}$$

to Eq. (2.33), rearranging the terms and using Eq. (2.29) the general wave equation (2.14) is converted into the form of an inhomogenous wave equation

$$\nabla^2 \tilde{\boldsymbol{E}} - \frac{\varepsilon_r}{c^2}\frac{\partial^2}{\partial t^2}\tilde{\boldsymbol{E}} = \frac{1}{\varepsilon_0 c^2}\frac{\partial^2}{\partial t^2}\tilde{\boldsymbol{P}}^{(\mathrm{NL})} . \tag{2.35}$$

This is otherwise the same equation as for the case of non-zero linear susceptibility in Section 2.3 (Eq. (2.26)), but now there is an additional nonlinear term on the right-hand side of the equation. The nonlinear polarization therefore acts as a source term for new electromagnetic field components.

2.5 Nonlinear interaction

In a dispersive medium the interaction between light and matter varies with frequency and hence the wavelength of light [9]. This is the case with many materials, and all the materials we consider in this study. Because the response depends on the frequency of the field, it is convenient to express the electric field at position $\boldsymbol{r}$ as the superposition of its frequency components ω_n

$$\tilde{\boldsymbol{E}}(\boldsymbol{r},t)=\sum_{\omega_n>0}\left(\boldsymbol{E}_n(\boldsymbol{r})e^{-i\omega_n t}+\boldsymbol{E}_n^*(\boldsymbol{r})e^{i\omega_n t}\right) \tag{2.36}$$

or in a more simple form

$$\tilde{\boldsymbol{E}}(t)=\sum_{\omega_n>0}\left(\boldsymbol{E}_n(\boldsymbol{r})e^{-i\omega_n t}+c.c.\right), \tag{2.37}$$

where *c.c.* stands for the complex conjugate. As $\tilde{\boldsymbol{P}}^{(\mathrm{NL})}$ depends on $\tilde{\boldsymbol{E}}$, the nonlinear polarization can also be expressed in a similar way as [10]

$$\tilde{\boldsymbol{P}}^{(\mathrm{NL})}(t)=\sum_{\omega_n>0}\left(\tilde{\boldsymbol{P}}_n^{(\mathrm{NL})}e^{-i\omega_n t}+c.c.\right). \tag{2.38}$$

As an example, we may consider the case where the electric fields has two frequency components ω_1 and ω_2 and the second-order susceptibility is the only significant nonlinear susceptibility tensor. The nonlinear polarization is then, according to Eq. (2.32),

$$\tilde{\boldsymbol{P}}^{(\mathrm{NL})}=\tilde{\boldsymbol{P}}^{(2)}=\varepsilon_0\,\boldsymbol{\chi}^{(2)}\tilde{\boldsymbol{E}}^2=\varepsilon_0\,\boldsymbol{\chi}^{(2)}\left(\boldsymbol{E}_1e^{-i\omega_1 t}+\boldsymbol{E}_1^*e^{i\omega_1 t}+\boldsymbol{E}_2e^{-i\omega_2 t}+\boldsymbol{E}_2^*e^{i\omega_2 t}\right)^2. \tag{2.39}$$

When this polarization is decomposed into its frequency components, five different equations are found as follows:

$$\tilde{\boldsymbol{P}}_{2\omega_1}^{(2)}=\varepsilon_0\,\boldsymbol{\chi}^{(2)}\boldsymbol{E}_1^2e^{-2i\omega_1 t}+c.c. \quad \text{(SHG)} \tag{2.40}$$

$$\tilde{\boldsymbol{P}}_{2\omega_2}^{(2)}=\varepsilon_0\,\boldsymbol{\chi}^{(2)}\boldsymbol{E}_2^2e^{-2i\omega_2 t}+c.c. \quad \text{(SHG)} \tag{2.41}$$

$$\tilde{\boldsymbol{P}}_{\omega_1+\omega_2}^{(2)}=2\varepsilon_0\,\boldsymbol{\chi}^{(2)}\boldsymbol{E}_1\boldsymbol{E}_2e^{-i(\omega_1+\omega_2)t}+c.c. \quad \text{(SFG)} \tag{2.42}$$

$$\tilde{\boldsymbol{P}}_{\omega_1-\omega_2}^{(2)}=2\varepsilon_0\,\boldsymbol{\chi}^{(2)}\boldsymbol{E}_1\boldsymbol{E}_2^*e^{-i(\omega_1-\omega_2)t}+c.c. \quad \text{(DFG)} \tag{2.43}$$

$$\tilde{\boldsymbol{P}}_0^{(2)}=\varepsilon_0\,\boldsymbol{\chi}^{(2)}\left(\left|\boldsymbol{E}_1\right|^2+\left|\boldsymbol{E}_2\right|^2\right)+c.c. \quad \text{(OR)} \tag{2.44}$$

Each of these equations refers to a certain physical phenomenon, as expressed with the abbreviations in the brackets. Hence, a non-zero second-order susceptibility can stimulate five new electric field components to an output field in addition to the two original components, as illustrated in Figure 2.1.

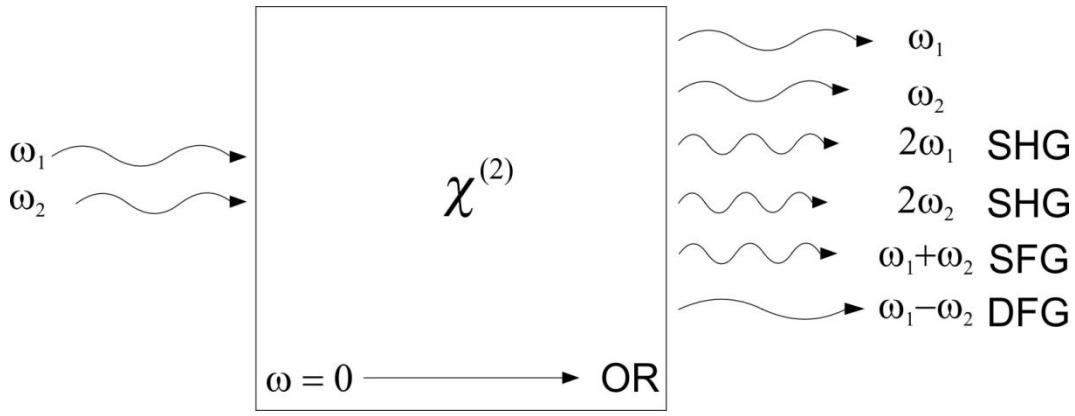

Figure 2.1. *Illustration of new frequency components when a material with non-zero second-order optical susceptibility is excited with input beams at two different frequencies.*

SHG is the process where the stimulated field has doubled frequency compared to one of the input frequencies. This is why the process is also called frequency doubling. SHG can be observed for both input frequencies ω_1 and ω_2. In sum-frequency generation (SFG), the output frequency is the sum of the two input frequencies. On the contrary, in difference-frequency generation (DFG) the output frequency is the difference between the two input frequencies. Unlike the other effects, optical rectification (OR) does not cause any electromagnetic radiation, but instead creates a static electric field within the nonlinear material. [10]

As shown above, when two sufficiently strong electric fields at different frequencies are applied on a sample with non-vanishing $\chi^{(2)}$, four new radiative fields with different frequencies can be generated. However, usually only one of the generated nonlinear effects is clearly observable at a time. This is because the efficient generation of a new polarization component occurs only if the so-called phase-matching condition is fulfilled, which is usually possible for only one frequency at a time. The phase-matching condition means that both the two excitation waves and one of the generated waves have almost the same phase. Otherwise, the energy flow is not only from the incident waves to the generated component, but also from the generated wave back to the original ones. Consequently, the intensity of the generated wave stays weak. [10]

A maximal crystal length useful in producing a nonlinear signal is called the coherence length. It describes over how long distance all the interacting waves are almost in the same phase. As perfect phase matching is impossible to achieve in a dispersive medium, where the speed of electromagnetic wave depends on its frequency, birefringent

materials are often used for maintaining the phase matching condition for the desired output signal. [10,15]

In addition to the effects mentioned above, NLO effects include also other phenomena, e.g., THG, two-photon absorption and stimulated Raman scattering. SHG and THG are the two most important effects for this Thesis and will next be more closely introduced.

2.6 Second-harmonic generation

In Section 2.5, the example of second-order nonlinearity was discussed for input fields at two different frequencies. However, if light of only one frequency is applied to a material with a non-zero $\chi^{(2)}$, the second-order polarization is, according to Eq. (2.32),

$$\begin{aligned}\tilde{\boldsymbol{P}}^{(2)} &= \varepsilon_0 \, \chi^{(2)} \tilde{\boldsymbol{E}}^2 = \varepsilon_0 \, \chi^{(2)} \left(\boldsymbol{E}_1 e^{-i\omega_1 t} + \boldsymbol{E}_1^* e^{i\omega_1 t} \right)^2 \\ &= \varepsilon_0 \, \chi^{(2)} \left(\left| \boldsymbol{E}_1 \right|^2 + \boldsymbol{E}_1^2 e^{-2i\omega_1 t} \right) + c.c.. \end{aligned} \tag{2.45}$$

Now OR and SHG are the only possible nonlinear phenomena as SFG and DFG are not meaningful processes with only one input frequency.

The energy-level diagram for SHG is shown in Figure 2.2. The bottom line illustrates the ground state of the nonlinear material and the dashed lines are so-called virtual states. This means that when two input photons with frequency ω are destroyed and one photon with a frequency of 2ω is produced, the material itself does not change its energy state. As no energy is left in the material, the process gives rise to no losses. Such a process is said to be coherent. [10] SHG is often used for converting laser light to another spectral region as the output signal has a wavelength that is equal to half of that of the input light. For example, with the help of SHG, visible light can be created from an infrared laser source. [10]

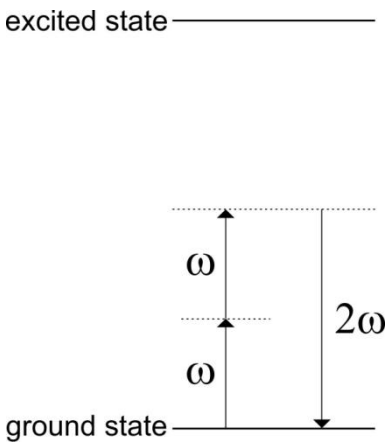

Figure 2.2. *Energy-level diagram describing the SHG process.*

Second-order nonlinear effects, as well as other even-order nonlinear effects are forbidden in materials possessing inversion symmetry. This means that in centrosymmetric media $\chi^{(2)}$ equals zero. This is a very strong rule, as 11 of 32 possible crystal classes are centrosymmetric. Nevertheless, at the surface of a material, the inversion symmetry is always broken. This is why SHG is a very powerful and widely used tool for studying material interfaces, surface effects, and thin films. [10] Furthermore, many biological tissues lack inversion symmetry, and in addition to interfaces, biological samples are a major focus of SHG applications [16].

2.7 Third-harmonic generation

One order higher nonlinear polarization is third-order polarization. It is described by the third-order susceptibility $\chi^{(3)}$, which is non-zero also in centrosymmetric media. The third-order nonlinearity is responsible, for example, for the phenomena called intensity-dependent refractive index (also called the optical Kerr effect) and four-wave mixing (FWM). [10] In this Thesis, however, we are interested mainly in THG.

The principle of THG is similar to SHG in the sense that in both processes the input beam consisting of only one frequency induces an output beam at another frequency. In THG, the output beam has a frequency three times the original and a wavelength of one third of the original. The energy-level diagram of THG is shown in Figure 2.3. Also in THG, the material itself is not excited and only virtual levels are used when three photons at frequency ω are destroyed and one photon at frequency 3ω is produced. Like SHG, THG is also a very practical tool in nonlinear microscopy especially for detecting transparent specimens. Likewise, it can also provide information from interfaces, but furthermore it provides a signal from a centrosymmetric bulk sample, too. [10]

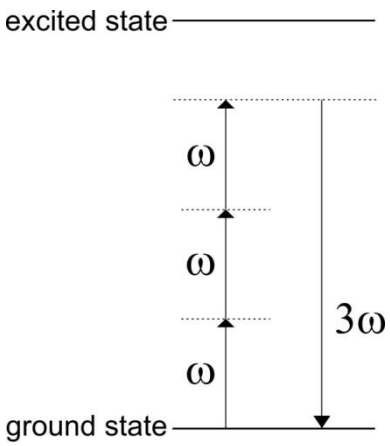

Figure 2.3. *Energy-level diagram describing the THG process.*

2.8 Polarization state of light

An electromagnetic wave propagating in the positive *z*-direction can also be described by the equation

$$\tilde{\boldsymbol{E}} = \hat{\boldsymbol{i}} E_{0x} e^{i(kz-\omega t)} + \hat{\boldsymbol{j}} E_{0y} e^{i(kz-\omega t+\Delta\phi)}, \tag{2.46}$$

where $\hat{\boldsymbol{i}}$ and $\hat{\boldsymbol{j}}$ are unit vectors in the *x*- and *y*-directions, respectively, E_{0x} and E_{0y} are the corresponding field amplitudes, *k* is the wave number, and $\Delta\phi$ is the phase difference between the *x*- and *y*-components of the field. If there is no phase difference, meaning that $\Delta\phi = 0$, the electric field is said to be linearly polarized and the electric field vector can be thought to oscillate back and forth along a fixed direction in the *xy*-plane. [9] Notice that this concept of the state of field polarization considered in this Section is different from the material polarization discussed earlier.

Linear polarization is only one of many possible polarization states of light. Another well-defined and important polarization state is circular polarization. When light is circularly polarized the phase difference between the *x*- and *y*-components is $\pi/2$ and their amplitudes are equal. The expression for the wave is then

$$\tilde{\boldsymbol{E}} = \hat{\boldsymbol{i}} E_0 e^{i(kz-\omega t)} + \hat{\boldsymbol{j}} E_0 e^{i\left(kz-\omega t\pm\frac{\pi}{2}\right)}. \tag{2.47}$$

When circularly polarized light propagates the distance of one wavelength, the tip of the polarization vector draws a circle as viewed from the beam axis. The rotation direction of the vector depends on the sign of the phase difference and light is said to be right- (RHCP) or left-handed circularly polarized (LHCP) depending on the direction of the rotation. [9]

The most general polarization state is elliptical polarization, where the phase difference and the ratio between the *x*- and *y*-components are arbitrary. Thus, Eq. (2.46) describes elliptically polarized light, and linear and circular polarizations are just special cases of elliptical polarization. Light is said to be unpolarized if it consists of beams with different polarization states, each with random phase and orientation. [9] Sunlight is an example of unpolarized light.

As mentioned earlier, in a birefringent material the interaction with medium and light depends on a propagation direction of light. Any electromagnetic wave can be expressed as a superposition of two field components perpendicular to each other. When a wave propagates in a birefringent medium, the velocity of these two field components may be different, and thus, a phase shift is induced between them leading to a change in polarization. By adjusting the orientation and thickness of the birefringent medium, the induced phase shift can be tailored. [9]

Wave plates are components made of a birefringent material and designed to change the polarization state of light in a particular way. A half-wave plate (HWP) changes the direction of linear polarization, while a quarter-wave plate (QWP) converts linear polarization to either elliptical or circular polarization depending on the angle between the direction of the linear polarization and the wave plate axis. [9] Both HWP and QWP are used in the microscopy setup of this Thesis.

2.9 Linear and nonlinear circular dichroism

A material is said to be optically active, or chiral, if it appears in two so-called enantiomers having different handedness, meaning that their mirror images cannot be superimposed onto each other [17]. Optical activity can originate from a molecular structure, arrangement of the molecules, or both of these [2]. Physical and chemical properties of the enantiomers are similar when they are in non-chiral environment, but in interaction with another chiral element they behave in different ways [18]. The other way round, the refractive index of a chiral material is different for LHCP and RHCP light as these two polarizations clearly have different handedness making them in some sense chiral probes.

As linear polarization can be thought to be a combination of LHCP and RHCP light with the same amplitude and frequency, the plane of linearly polarized light is rotated during its propagation through a chiral medium [19]. Another important property of optically active media is that the absorption coefficients for different circular polarizations are not equal. This phenomenon is called circular dichroism (CD) [20]. CD can be understood in terms of the imaginary part of the refractive index, which is related to absorption properties of a medium [10].

In linear optics, CD is mostly used as a spectroscopic tool by measuring the differences in absorbance ΔA for the two circular polarizations (A_{LHCP} and A_{RHCP}) at different wavelengths [20]

$$\Delta A(\lambda) = A_{LHCP}(\lambda) - A_{RHCP}(\lambda) . \tag{2.48}$$

This phenomenon has many applications especially in biology. For instance, conformational changes in proteins can be investigated with CD spectroscopy [20]. Nonlinear CD phenomena were theoretically predicted in the 1980s [21], and the first experimental extension of CD spectroscopy to the nonlinear region was made in 1993 with FWM and SHG by using solution samples. In these demonstrations, the CD response was taken as the difference in the nonlinear signal by using LHCP and RHCP light for excitation. [22,23] Soon after that, nonlinear CD techniques were used for biological molecules for the first time [24]. The advantages of nonlinear CD over linear CD are, for example, much better contrast, sensitivity and the fact that only surfaces can be detected instead of the whole bulk sample [24].

Recently SHG-CD has been used in microscopy, for example, to investigate the 3D orientation of collagen fibres in tissues, as their disorder can be linked to certain diseases [25]. Hence, the CD effect is not used only as a spectroscopic tool anymore, but also as a microscopic tool. The CD response can be expressed with intensities [25]

$$I_{CD} = \frac{I_{LHCP} - I_{RHCP}}{\left(I_{LHCP} + I_{RHCP}\right)/2}. \tag{2.49}$$

Thus, for example in the SHG-CD microscopy, the CD-signal in each image pixel is the difference in SHG intensities between the signals excited with different circular polarizations divided by their average. The CD response for THG can be calculated in the same manner, just by replacing the SHG intensities with THG intensities. For now, THG-CD microscopy is, however, not as widely used tool as SHG-CD. In fact, it was only recently demonstrated both theoretically and experimentally for biological molecules [14,26].

3. NONLINEAR OPTICAL MICROSCOPY

3.1 Introduction to microscopy

Human beings can naturally distinguish two objects separated by a distance of about 0.1 mm, which is around the average diameter of a human hair. This distance is called the resolution of the human eye. An instrument used for viewing images with a resolution smaller than 0.1 mm is called a microscope. In other words, a microscope is an optical device used for obtaining a magnified image of a small object. The first scientific microscopes were made in the end of the 16^{th} century. [3]

In traditional microscopes, the image is formed with a lens system and relies on visible light that is reflected, scattered or fluoresced from the object and detected with the eye or a camera [3,27]. The distinction of the target object from the background as well as the details inside the sample can be seen because different materials have different optical properties [20].

However, light is not the only way to obtain magnified images. For example, in electron microscopy a beam of electrons interacts with matter and thereby provides information about the sample. Electron microscopy provides better resolution than optical microscopy because of the shorter wavelength range of electrons when compared to light. The first electron microscopes were developed in the early 1930's. [3] Even if electron microscopy has very good resolution, optical microscopy is still an important method especially in sciences related to biology as it can be used to investigate living samples in their natural environments [28].

3.2 Nonlinear microscopy

Traditional optical microscopes are based on linear optical effects. However, in this Thesis, the focus is on nonlinear optical microscopy (NLOM), which embraces all techniques that rely on NLO effects to establish image contrast. The main goal is the same as in linear microscopy, to visualize small objects that cannot be resolved by the unaided eye. The fundamental difference compared to traditional optical microscopy is that in NLOM, the measured quantity is not scattered, reflected or fluorescent light, but the light generated in the target object due to nonlinear interactions. [29] Furthermore, it is possible to use wavelengths outside of the visible spectrum. For instance, infrared light is often used in nonlinear microscopy.

In NLOM techniques, the target is usually excited by a focused laser beam, as the nonlinear response exists only at locations where the input light intensity is very high. As also mentioned earlier, the nonlinear response is proportional to a high power of the

excitation light intensity. As a result of these two effects, the observed nonlinear signal originates only from a small volume at the focal point of the incident field and out-of-focus contributions are almost non-existent. [5] This makes it possible to image not only surfaces, but also objects inside the sample and thus produce 3D images [16]. The best penetration into biological samples is achieved with near infrared wavelengths, e.g., penetration to a depth of 500 μm is achievable in SHG microscopy [16,30]. 3D imaging is also possible in linear microscopy by using confocal techniques, where out-of-focus light is excluded from the detector with a spatial filter, like a pinhole, in the focal plane of the focusing lens [20]. However, linear microscopy usually uses shorter wavelengths than nonlinear microscopy, and thus the penetration length into biological tissue is not as good as in nonlinear microscopy.

As the signal in nonlinear microscopy always originates from a very small volume, it is not possible to image the whole sample area at once. Scanning over the area under consideration is therefore necessary. This approach is called laser scanning microscopy, where the picture of the sample is constructed by going through the sample area point by point, thus producing a raster pattern. The movement between the sample and the beam can be executed either by moving the sample stage in relation to a stable excitation beam or by using mirrors to move the excitation beam along the sample surface. [20] 3D imaging can be performed by changing the relative position of the sample and the excitation beam not in the plane of the sample surface but in the direction of the excitation beam and repeating the raster scanning with different depths.

The development and huge progress in confocal microscopy and laser techniques during the last decades have provided the basis for developing NLOM methods [30]. Earlier, most of the applications of NLOM were in engineering, but nowadays NLOM is a widely-used research technique also in biology [5,30]. It provides a spatial resolution down to sub-micrometric regime and temporal scales even down to femtoseconds. As mentioned earlier, NLOM also allows deeper penetration into the sample material and higher signal-to-noise ratio than linear techniques. There are a vast number of different kinds of NLOM techniques, such as two-photon excited fluorescence (TPEF), THG, SHG, SFG, coherent anti-Stokes Raman scattering and FWM, each of them having their own application targets. [16,30] For certain purposes, it is also profitable to combine two or more different NLOM techniques, such as TPEF, SHG and THG, and it is also possible to use NLOM and some other imagining modalities together [5,31,32]. In addition to its biological applications, NLOM is nowadays also used for imaging of artificial nanomaterials such as gold nanoparticles and carbon nanotubes [7,33-37]. For instance, the samples used in this Thesis are gold nanoparticles.

3.3 Linear and nonlinear fluorescence microscopy

Single-photon excited fluorescence (SPEF) microscopy is an example of linear optical microscopy. In fluorescence, a molecule, called a fluorophore, absorbs a high-energy photon and, after a short delay, emits another photon with lower energy. The loss of

energy is due to non-radiative vibrational relaxation between the final state of absorption and the initial state of fluorescence transition. This is illustrated in Figure 3.1. In fluorescence microscopy, the emitted fluorescence signal is detected and thus, for example, the movement of molecules in cells can be investigated. [38] Fluorescence is not the only way for an excited molecule to return to its ground state. However, the wavelength of fluorescent light corresponds roughly to the energy difference between the ground state and the excited state, being thus almost constant for a given molecule. Hence, the fluorescence signal is easy to distinguish from other spectral components of radiation by using filters suitable for discriminating the fluorescence from the excitation.

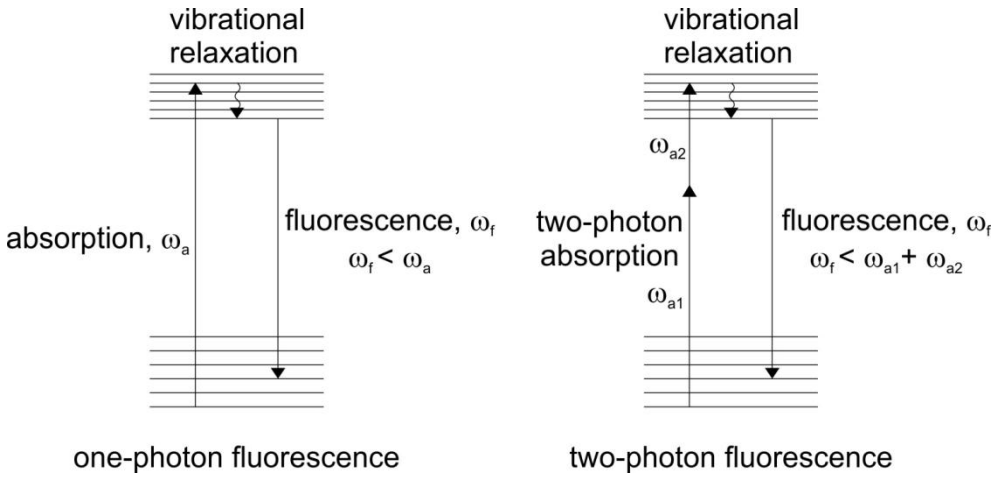

Figure 3.1. *Illustrations of single- and two-photon fluorescence phenomena. Horizontal lines indicate vibrational states and ω are frequencies.*

The nonlinear counterpart for fluorescence is TPEF. The idea is much the same as in one-photon fluorescence explained above but in TPEF the excitation to the high-energy state is caused by almost simultaneous absorption of not only one, but two photons. The sum of the energies of these two photons has to equal the energy difference between the ground state and the excited state. The principle of TPEF is also illustrated in Figure 3.1. As the absorption of the two photons has to be almost simultaneous, the probability for this phenomenon to occur is usually very low, practically zero under at ambient conditions. However, by focusing a pulsed laser beam on the sample, a sufficiently high photon density can be achieved for TPEF to occur. Thus, the probability of TPEF in the tiny focal volume is relatively high, but outside the focal volume it decreases rapidly. This allows for better resolution imaging compared to SPEF, as in TPEF the fluorescence comes only from the desired location. [38]

Figure 3.2 shows a fluorescence signal from a sample cuvette for the cases of SPEF and TPEF. It is evident how SPEF signal originates from the entire path of the excitation beam through the cuvette, whereas the TPEF signal is created only at the focus. In addition to its resolution, another advantage of TPEF is that the longer wavelength used

for excitation allows for deeper penetration into highly scattering tissues, like living cells, than what is achieved with traditional fluorescence microscopy [16].

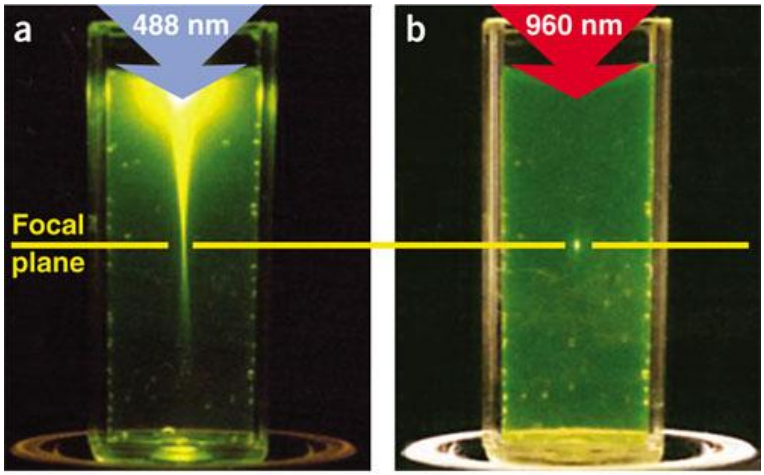

Figure 3.2. *In SPEF (a) the signal originates from the whole excitation path through the sample, whereas in TPEF (b) the signal comes only from the small focal volume. [39]*

Some molecules have natural fluorescence and are said to be autofluorescent and some can be modified to make them fluorescent. However, it is often necessary to perform measurements on sample molecules without fluorescence ability and, hence, an additional label substance is needed. [29] The benefit of external label materials is that they can be engineered for the used excitation wavelengths and for attaching to the desired target molecules [5]. The addition of dyes can be done by injecting label molecules to target cells or by extracting cells from a sample, adding labels to them and returning them to the sample. These techniques are called *in vivo* and *ex vivo* labelling, respectively. [29] If different kinds of fluorophore labels are used, many kinds of phenomena can be detected at the same time.

Using labels is necessary in many cases of fluorescence imaging, but in general it is preferable to avoid the use of labels. The external substances in cells cannot only be toxic or harmful for living organisms, but they may also have an influence on the measured quantity or process. This can even complicate the implementation of the measurements and interpretation of the results. [5]

As examples of TPEF images, Figure 3.3 shows the image of human normal and cancerous oesophageal submucosa [40]. In oesophageal submucosa, the autofluorescing protein called elastin is very abundant, and in normal tissue it exhibits a strong fluorescent signal (Figure 3.3a)) [40,41]. However, due to cancer, drastic changes in the occurrence of elastin are evident as shown in Figure 3.3b).

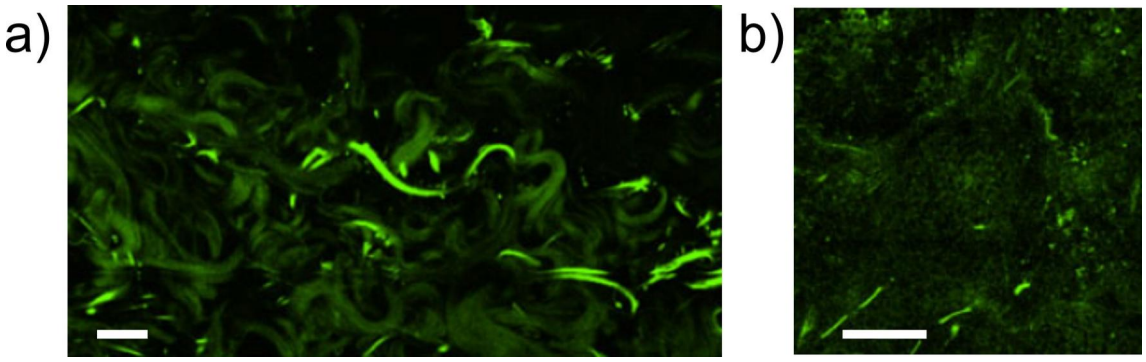

Figure 3.3. *TPEF images of healthy (a) and cancerous (b) oesophageal submucosa. Scale bars are 20 μm (a) and 100 μm (b). [40]*

3.4 Second- and third-harmonic generation microscopy

In this Thesis, the microscopy techniques under consideration are SHG and THG microscopy. SHG was introduced as a microscopic tool for the first time in the 1970's to visualize crystalline structures [16]. The SHG signal is mainly emitted to the forward direction, but in some cases the backward signal is also measurable. This is a significant advantage in some applications, such as *in situ* and *in vivo* measurements of biological organisms where the measurements are done directly from the body without extracting a biopsy. [5,31] SHG as well as other harmonic techniques seem to have a promising future in biological and especially biomedical applications as a diagnostic tool. This is because many biological molecules, such as the most abundant protein in the human body, collagen, are not centrosymmetric and thus produce a detectable SHG signal [32]. Figure 3.4 shows an example of a SHG image from oesophageal submucosa, where collagen is the source of the SHG signal. The samples used are the same as in Figure 3.3, and, as before, healthy tissue produces much stronger signal than cancerous tissue.

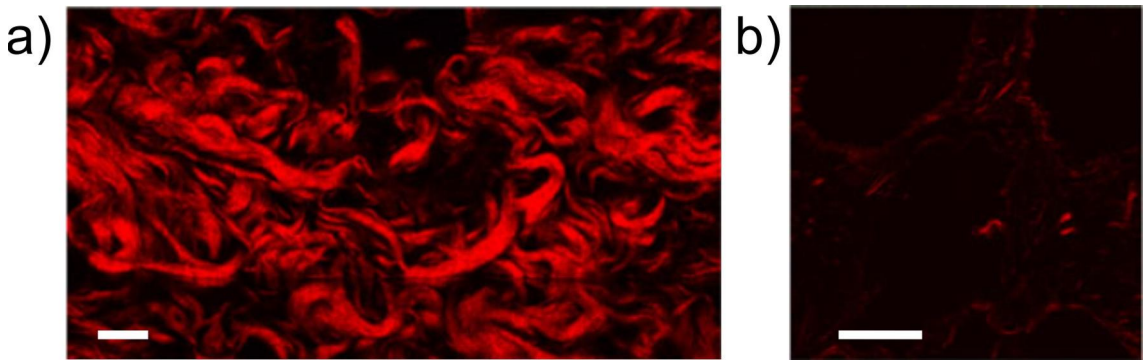

Figure 3.4. *SHG images of healthy (a) and cancerous (b) oesophageal submucosa. Scale bars are 20 μm (a) and 100 μm (b). [40]*

THG also has its own specific applications in microscopy. It can be used for imaging anisotropic centrosymmetric materials and interfaces in homogenous media [16]. One important application for THG microscopy is investigating lipids in cells and tis-

sues, as lipids are the main source of THG in living cells. For instance, when combined with TPEF and SHG, lipid interactions with the cell environment can be observed. [6]

On the other hand, THG is also used for imaging proteins. Figure 3.5 shows an example where human lung tissue is imaged simultaneously with THG and TPEF. This is done because the aim was to show that one important THG source in tissue is elastic fibers. As can be seen in Figure 3.5, the THG signal (blue) correlates excellently with the TPEF signal (magenta) originating from elastin.

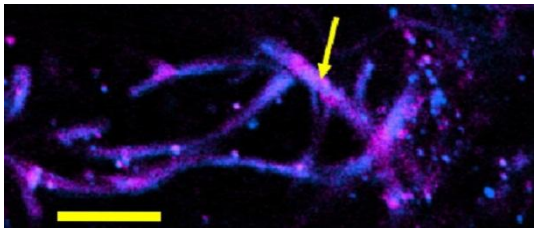

Figure 3.5. *THG (blue) and TPEF (magenta) images of human lung tissue. The yellow arrow represents the location of elastic fiber. Scale bar = 20 μm. [41]*

Like TPEF, SHG- and THG-based imaging techniques allow submicron resolution and relatively deep penetration into biological tissue [16,32]. However, the advantages of SHG and THG when compared to TPEF and many other imaging techniques are that the signal originates from the natural organization of molecules, thus making the techniques label-free. Furthermore, as both SHG and THG are coherent processes they do not excite the molecules of the sample [16,32]. Thus, they can be relatively easily applied to living cells without damaging them drastically. However, the intense laser power needed for making the nonlinear effects to occur can be harmful for samples under illumination. This drawback can be minimized by using, not continuous, but pulsed laser beams. Then the average power is lower than what would be needed if a continuous-wave (CW) beam was used.

3.5 Polarization-resolved and circular dichroism microscopy

Manipulation of the polarization state of input light gives an additional degree of freedom to be utilized in NLOM. For example, by controlling the polarization of the input beam, we can get information about the orientation of molecules and investigate the molecular angular distribution in the sample. This is important information for many biological systems and difficult to gain by other methods. Polarization-resolved SHG microscopy can also be used for structural investigation of some biological samples such as collagen or acto-myosin. Polarization-resolved THG imaging is used, for example, to observe heterogeneities in corneal tissues. [16]

One possibility to utilize different polarizations in microscopy is to perform CD measurements. As nonlinear CD can provide a higher contrast than linear CD and nonlinear microscopy itself has many other advantages over linear microscopy, the combination of nonlinear CD and microscopy has lately given rise to promising results. For

example, investigation of collagen with SHG-CD has been shown to give good results and can probably be implemented as a clinical diagnostic tool for some diseases. [25,42] Also, SHG-CD microscopy for 3D imaging has been demonstrated [43].

Figure 3.6 shows an example of SHG-CD microscopy image from mouse tendon illuminated with RHCP (Figure 3.6a)) and LHCP (Figure3.6b)) light. The corresponding CD response is shown in Figure 3.6c). [42] The overall morphology seems to be similar in both Figures 3.6a) and 3.6b). However, the SHG intensities are not equal for both polarizations, which is clearly seen in Figure 3.6c) as variations in colours and the difference of 5 % for the CD response is found. This difference is relatively small, but promises that SHG-CD could in the future be used as a diagnostic tool as the CD response varies depending on the collagen orientation in tissue [42].

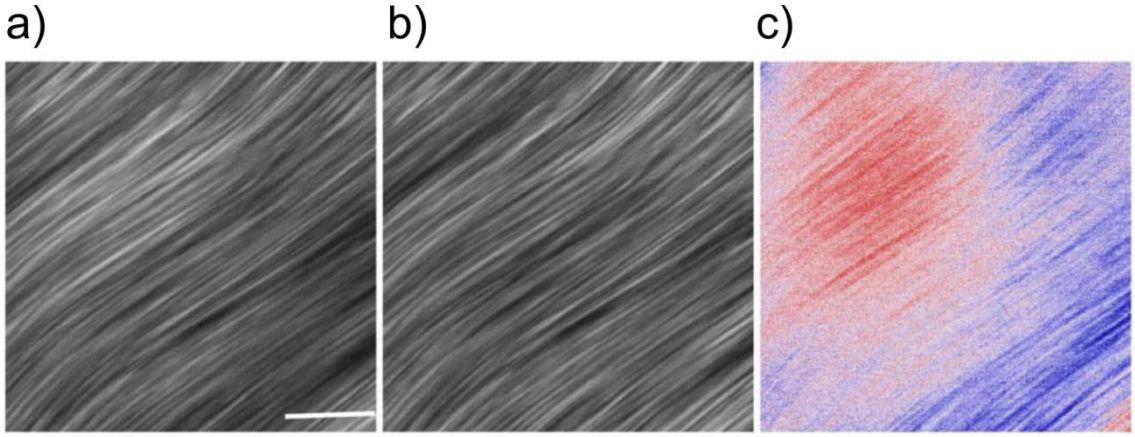

Figure 3.6. *SHG images of mouse tendon measured with RHCP (a) and LHCP (b) light. The corresponding SHG-CD response (c) shows the intensity differences between a) and b). Scale bar = 25 μm. [42]*

3.6 Plasmonic metamaterials

Metamaterials are man-made materials with sub-wavelength structural dimensions. Thus, they can often have properties not found in nature. The term metamaterial has only been used for about 15 years, but such materials have existed even in ancient history and they have already been studied for decades. Metamaterials exhibiting tailored electromagnetic responses at optical frequencies are called optical or photonic metamaterials. Research in this area is very active and concentrated on many themes such as giant artificial chirality, nonlinear optics and electromagnetic cloaks for invisibility. [44]

The field of metallic nanostructures and their applications is called plasmonics. Plasmonic metamaterials are thus tailored and artificially made metallic nanostructures. Their optical properties result from the coupling between the incident electromagnetic field and free-electron movement at the surface of the metal [37]. When light interacts with metal nanostructures, resonances called plasmons or surface plasmons are generat-

ed [45]. In general, surface plasmons are electromagnetic waves propagating along the interface between a metal and a dielectric material [20].

For metal nanoparticles, these interactions are mostly observed only in the vicinity of the particles and are thus called localized surface plasmons, which are dependent on the particle size and shape [37]. Thus, by tailoring the details of nanostructures, their optical properties can be modified. Nonlinear effects are very sensitive to changes in the excitation field and thus only small modifications in the nanostructure can affect the generated nonlinear signals significantly [46]. Plasmonic metamaterials will in the future result in smaller optical components and allow very fast control of optical signals. They are investigated for producing new applications and also because they can provide new tools for enhancing nonlinear interactions. [37]

Chiral plasmonic metamaterials (CPMs) consist of a two-dimensional array of periodically arranged chiral structures on the scale of tens or hundreds of nanometers. They are typically fabricated on a metal-on-dielectric structure by electron-beam lithography or ion beam milling. CPMs have many unique optical properties because their chiral nanostructured grating gives rise to surface plasmon resonances with a very strong optical activity and CD effects. Thus, for example, ultrasensitive detection and characterization of proteins adsorbed on CPMs is possible. [47] The samples used for testing the microscopy program created in this Thesis were CPMs. They are introduced in more detail in Chapter 6.

4. MICROSCOPY SETUP

4.1 Overview of nonlinear microscopy setup

An imaging system is useless if it cannot produce high contrast images. In nonlinear microscopes, there are many factors affecting the image formation. First of all, the laser and its characteristics have to be suitable for the task at hand. Examples of typical laser specifications that affect image formation are, for instance, wavelength, pulse width, average power, and the polarization of the beam.

Aside from the laser source, another important factor in the imaging system is the microscope objective, which is used to deliver or focus the excitation beam to sample. Presently, there are many different kinds of objectives available, and it has to be chosen so that the properties of the objective are optimized to the used measurement arrangement. For example, the size of the resulting focal spot formed at the sample determines the 3D resolution of the system. Here, the numerical aperture of the objective plays a major role as the other important factor is the used excitation wavelength. Other factors that influence the image formation are, for example, the coherence length and the detection geometry of the imaging system. [48] Furthermore, in scanning microscopy the precision of the scanning system is essential.

In our nonlinear microscopy setup, the beam used for illuminating the sample is obtained from a mode-locked femtosecond laser. In principle, the laser beam is directed to the sample and the generated nonlinear signal is collected and subsequently measured. However, in order to get the beam from the laser to the sample in the desired form and, furthermore, the measured results to a computer, many different kinds of optical and mechanical components are needed. The simplified schematic figure of the setup used in the measurements of this Thesis is shown in Figure 4.1.

As can be seen from Figure 4.1, besides the laser, the sample plate and the detectors, other optical components such as wave plates, beam splitters, lenses, polarizers, mirrors, and filters are utilized in the beam path. These components are used for routine cleaning of the beam, that is, for magnification and collimation, polarization selection and wavelength discrimination. In the next Sections, the most important components of the setup are introduced and discussed in detail. Correspondingly, the program made for implementing the scanning microscopy measurements is described in Chapter 5.

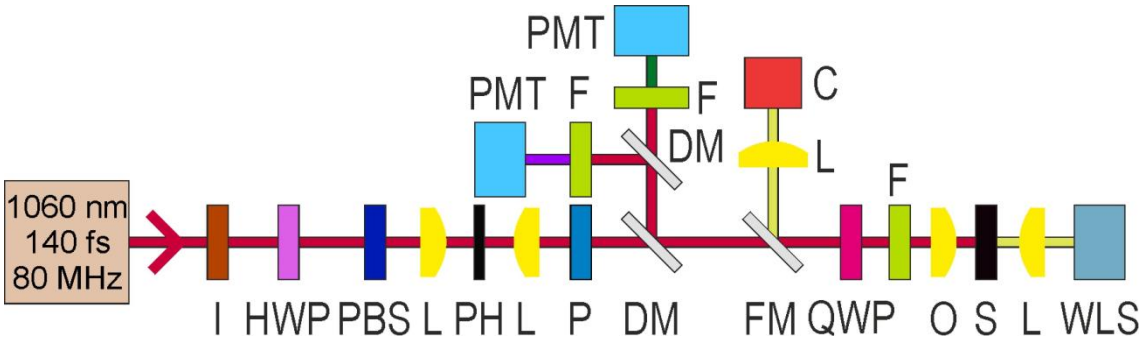

Figure 4.1. *A schematic of the microscopy setup. The left most component represents the laser and the others are labelled in the following way: I = Faraday isolator, HWP = half-wave plate, PBS = polarizing beam splitter, L = focusing or collimation lens, PH = pinhole, P = polarizer, DM = dichroic mirror, QWP = quarter-wave plate, F = spectral filter, O = objective, S = sample plate, PMT = photomultiplier tube, WLS = white light source, FM = flip mirror, C = camera.*

4.2 Laser

In nonlinear microscopy, a pulsed laser is used as the excitation light source. In our set-up, the laser is a Coherent Chameleon Vision Laser, which is a wavelength-tunable, mode-locked, diode-pumped pulsed laser with Ti:Sapphire as gain medium. The output wavelength range of this laser is 680-1080 nm. The pulsed laser beam exhibits a pulse width of about 140 fs and a repetition rate of 80 MHz. The average output power of the laser depends on wavelength, but it can be as high as 4 W at the wavelength of 800 nm. At the wavelength used in this Thesis, which is 1060 nm, the average power output of the laser is close to 500 mW. For comparison, the power of a normal laser pointer is a few milliwatts. The laser system has a built-in spectrometer for observing directly the output wavelength and average power.

The laser also needs a very stable environment to work properly. The Chameleon Vision Laser contains two systems for maintaining that. One is a chiller for cooling the laser head instruments and one is a Miniature Recirculating Unit (MRU). The MRU is used for cleaning, conditioning and dehumidifying the air inside the laser head. The room temperature in the laboratory room is also kept constant.

4.3 Propagation and spatial filtering of beam

Directly after the laser, a Faraday isolator is used to prevent backscattered light from the remaining part of the setup from entering the laser cavity. The output power of the laser is very high, up to 4 W, and cannot be directly controlled by the laser settings without causing a loss in the quality of the output beam properties. However, for our purposes, the intensity of the beam needs to be lowered to only a few milliwatts before reaching the sample. This is done with a HWP in tandem with a polarizing beam splitter (PBS).

The PBS is a component that divides the beam to horizontally and vertically polarized beams. When changing the polarization of the input beam with a HWP the relation between its vertical and horizontal components is varied, and thus the intensity of the beam transmitted by the PBS can be controlled. The unwanted beam that emanates from the PBS is blocked for safety reasons.

Ideally, the transverse shape of the laser beam has a Gaussian profile. However, dust and imperfections in lenses and mirrors may cause unwanted inhomogeneities and deviations in the expected beam profile. A spatial filter is used for cleaning the transverse profile of the beam back to the Gaussian shape. [9] The spatial filter has two lenses and a pinhole between them. The principle of a spatial filter can be understood in terms of Fourier optics.

In a spatial filter the first lens focuses the laser beam and a Fourier transformation of the beam is formed at the back focal plane of the lens. There each point corresponds to a single spatial frequency of the beam so that the higher the frequency the longer is the distance from the center of the focus. [15] The unwanted field components in the beam mostly have higher frequencies compared to the desired Gaussian beam. The pinhole placed at the focal plane of the first lens acts as a low-pass filter, hence preventing the unwanted high-frequency field components to continue their way and passing only the Gaussian shaped beam. [9] The second lens is located at its focal length from the pinhole and, thus, it collimates the cleaned beam, which can after that be furthermore modified and finally guided to the sample. A schematic figure of a spatial filter is shown in Figure 4.2.

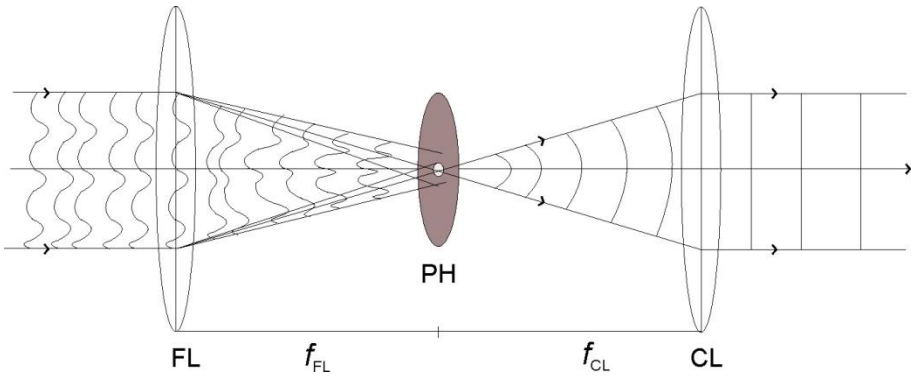

Figure 4.2. *Schematic of a spatial filter. An incident beam with imperfections (left side) is focused by a focusing lens (FL) to the pinhole (PH), and the cleaned beam is collected by a collimating lens (CL). The pinhole is located at the focal length (f_{FL}, f_{CL}) from both lenses.*

Our setup is built for polarization-resolved nonlinear microscopy. Thus, the option to control the polarization state of the input light is essential. The polarization control is implemented by manual or automated rotation of a QWP. Here, the rotation is performed with a Newport SR50CC Rotation Stage, which is controlled by a Newport ESP301 3-Axis Motion Controller. To ensure that the light passing through the QWP has originally only one known polarization, a polarizer is used before the QWP. After

the QWP, a filter for preventing the SHG light originating from the microscopy components to disturb the results is also used.

Right before the sample, there is a high numerical aperture microscope objective, which is needed for tightly focusing the laser beam to the sample [5]. In our setup the objective is a Nikon CFI LU Plan Fluor EPI P with 50x magnification and a numerical aperture of 0.8. This objective is designed to be used as an excitation lens for collimated input beams with wavelengths on the visible and infrared regions. It can be used in many kinds of microscopy setups including bright and dark field as well as polarization microscopy. The objective minimizes the chromatic aberrations for collimated input beams and has very low birefringence, necessary when polarized light is used.

If the transmitted nonlinear signal is to be measured, a collimation lens after the sample is necessary. When measuring the reflected signal, as is made in this Thesis, the excitation objective also acts as the collimation lens for the nonlinear signal. Then, the nonlinear signal is directed to its respective arm and furthermore to the detector with mirrors and filters suitable for the scattered wavelength detected. Before the measurements, the sample is located at the focus with the help of a camera. For this purpose, a white light source is needed for illuminating the sample, and the scattered light is directed to the camera with a flip mirror, which is placed in the setup only when the camera is used.

4.4 Sample scanning

As mentioned earlier, our aim is to perform scanning microscopy. This naturally requires the possibility to change the positions of the beam and the sample in relation to each other. In our setup, this is executed by moving the sample with respect to a fixed beam. The sample movement is performed with a Mad City Labs, Inc. 3-axis nanopositioning system. The specified motion ranges and resolutions of the scanning stage of this system are 75 μm and 0.2 nm, respectively, in the *x*- and *y*-directions and 50 μm and 0.1 nm in *z*-direction. The movement of the stage is controlled by a NanoDrive® 85 controller. The nanopositioning system is placed on a two-axis manual micropositioning stage so that more robust movement of the sample perpendicular to the beam is possible. The total movement of the micropositioning stage can be 50 mm per axis.

The nanopositioning system is based on piezoelectric actuators. The piezoelectric effect is a phenomenon in which material changes its physical dimensions upon the application of an electric field [49]. In our case, the movement command from the control program is turned into an electrical signal which in turn causes the piezoelectric material to expand or shrink and thus the positioner to move. The movement can be done in each dimension individually.

4.5 Detection of signal

A photomultiplier (PMT) is a device utilizing the photoelectric effect for photon detection. In practice, a PMT is a vacuum device consisting of a photocathode, series of dynodes and an anode. When a photon strikes the photocathode, a photoelectron is emitted and accelerated through the dynodes to the anode. The dynodes are made from a material providing secondary electron emissions for each electron striking them, resulting in a huge intensification (about 10^7 times [50]) of the electric signal. Furthermore, the process is very fast, and thus the small current caused by one photon at the cathode is almost immediately observed many times stronger at the anode [9]. In Figure 4.3 there is an illustration of the structure of a PMT. It is important that the PMT has an integrated cooling system, as the probability of thermal emission of electrons, an important error source, is then decreased drastically. In our setup we use a PMC-100-0 cooled high-speed photomultiplier tube produced by Becker & Hickl GmbH for detecting the non-linear signal emitted by the sample.

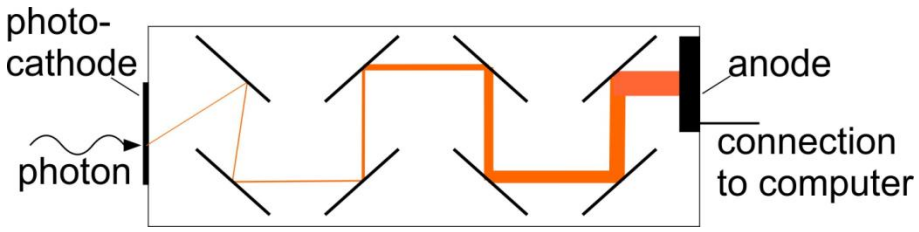

Figure 4.3. *Illustration of one possible configuration of a PMT. The width of the beam describes the number of electrons in it. Adapted from [50].*

The PMT output has to be analysed for producing useful results. One option for analysing the PMT output is the use of analog signal acquisition. In that method the random output signal from the PMT is smoothened with a low pass filter producing a continuous signal. [50] However, this is not the best solution for our purposes, as the signals we measure are assumed to be relatively weak. The output signal of the PMT therefore mostly consists of single pulses. When the number of these pulses within a certain time interval is measured by a counter/timer combination, the process is called photon counting. [50,51] The difference between the outputs of these methods is outlined in Figure 4.4.

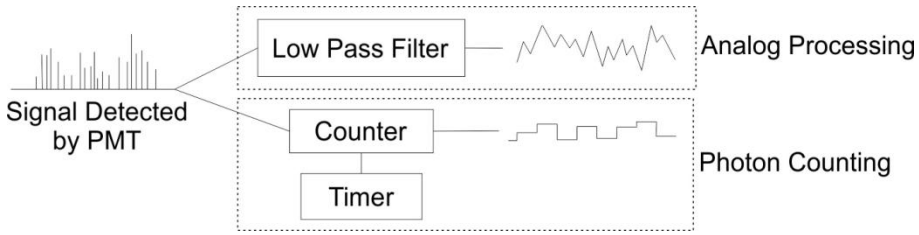

Figure 4.4. *Difference between the processing protocols of analog signal acquisition and photon counting. Adapted from [50].*

There are several benefits in photon counting when compared to the analog solution. One of them is stability. PMT gain stability is often a problem and analog solutions are sensitive to that, while photon counting is almost resistant against it. [50,51] Another important factor in all measurement devices is the signal-to-noise ratio, which is better in photon counting than in analog acquisition. In photon counting, the signal baseline drift is not a problem as only single pulses are counted instead of detecting the waveform. For the same reason, photon counting is also resistant to amplitude jittering caused by the random nature of the gain process in the PMT. An important feature of photon counting is that all output signals are not taken into account, but the threshold can be set so that background noise is excluded from the results. [50] This is illustrated in Figure 4.5.

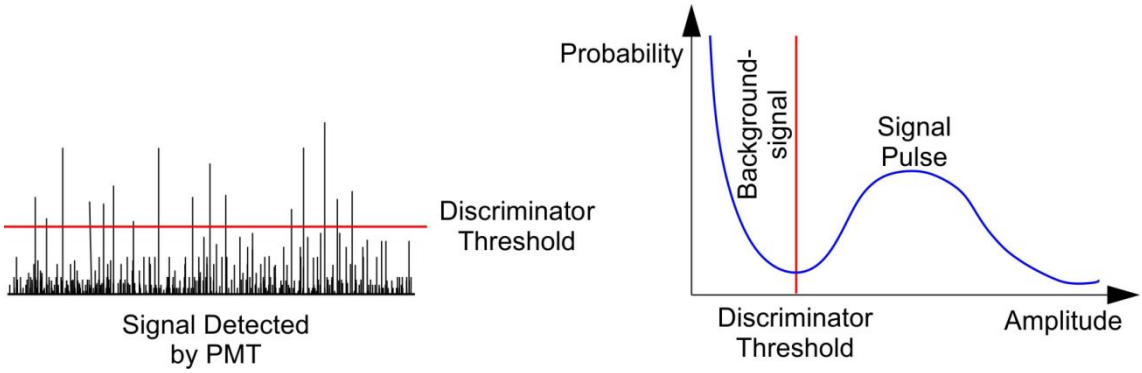

Figure 4.5. *By careful setting of the threshold amplitude the background noise can be excluded from the results in photon counting. Adapted from [50].*

In our setup, the PMT is integrated with a PMS-400A photon counting and multiscaler device produced by Becker & Hickl GmbH. The block diagram of the device is shown in Figure 4.6. The device can be used with two channels, so that, for instance, transmitted and reflected SHG light, transmitted and reflected THG light or both reflected or both transmitted SHG and THG light can be measured at the same time. The counting inputs Inp A and B are connected to the outputs of the PMTs and they receive the pulses caused by single photons striking the PMT cathode. The discriminator after the input is used for picking up and forwarding only the pulses exceeding the chosen threshold value. Gates A and B and their discriminators are used for receiving and delivering the gate pulses used for time-correlated single photon counting. These pulses are not used in our measurements. The control of the module is performed by a control logic circuit in conjunction with a timer circuit, where the latter takes care of measuring the desired time intervals. [50]

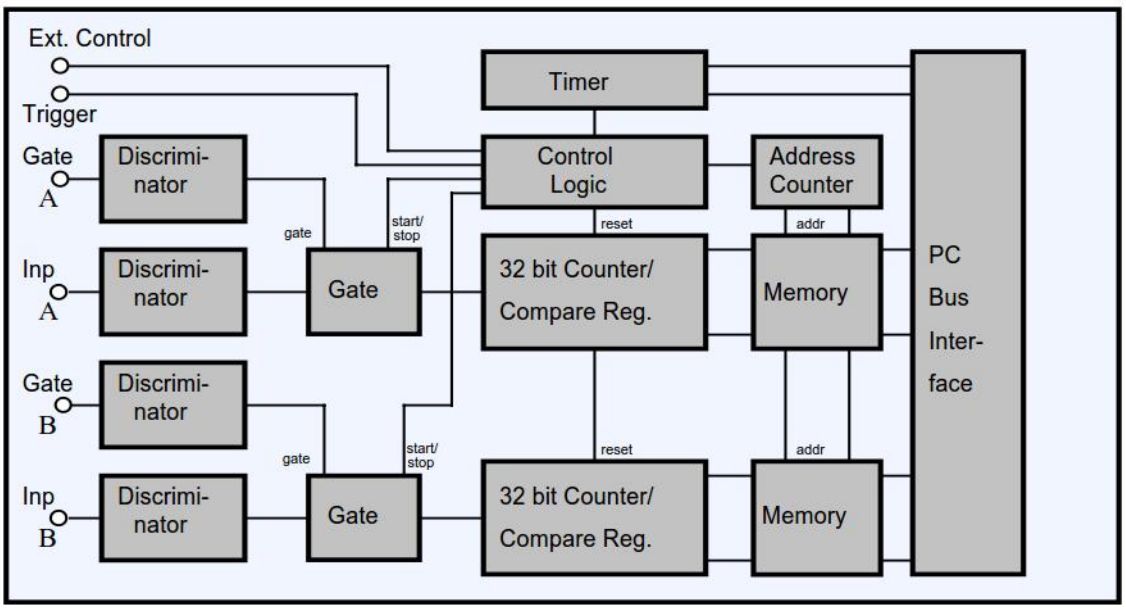

Figure 4.6. *Block diagram of a PMS-400A Photon Counter and Multiscaler. [50]*

There are three possible measurement modes in the PMS-400A device: 'channel rates', 'multiscaler' and 'event' modes. In the channel rates mode, the counter results are shown as bar diagrams for each channel at the end of each collection time interval. We use the multiscaler mode, where the counter results for collection time intervals are stored in the memory and can be later loaded separately from there to the computer. In the multiscaler mode, the number of photons is saved for every collection time interval, even if there were no events at all. In the event mode, the number of counts is stored only if sufficiently high number of photons are detected within the collection time interval. The threshold level is set by the user. [50]

In the setup of this Thesis, two identical PMTs were used. They were used for measuring SHG and THG signals, which have different wavelengths. PMTs have a certain spectral range, but the photons with wavelength inside that range are detected in general with equal efficiency. The separation of the signals with different wavelengths was made with appropriate filters. First, the collected beam from the sample was divided into two arms, one for measuring the SHG and another for measuring the THG signal. Then, in both arms there are two filters. In the SHG arm, the first filter allows photons with wavelengths between 400 and 900 nm to pass, and the second filter is tailored to pass only the photons around the SHG wavelength. In the THG arm the first filter allows both SHG and THG light to pass, but the second filter transmits only the THG photons. More detailed information about the used filters is given in Section 6.4 and in Appendix 1, which includes the specifications of the used filters.

5. USER INTERFACE FOR NONLINEAR MICROSCOPE

5.1 Integration and synchronization of devices

A nonlinear microscopy arrangement necessarily has many electronic devices that need to be controlled and moved before, during, and after a measurement sequence. For example, the QWP used for controlling the polarization of the input beam could be set manually for each measurement separately. However, for accuracy and easiness, a computer controlled motor is used for changing the angle of the QWP. Usually there is a control program delivered with electronic laboratory devices, and in principle nonlinear microscopy could even be done without any general microscopy program at all. On the other hand, there are also available commercial microscopy systems, where all the desired devices are built-in.

For our needs, however, the most suitable solution was to build the whole microscopy setup to our own needs. For ease of use and for synchronizing the used instruments during a measurement sequence, the control of electronic devices in the microscopy setup is integrated into a single program. The design and implementation of that program and its user interface were the main targets of this Thesis. The program was implemented by LabVIEW which is a graphical programming platform designed for engineers and scientists to build and control a wide range of applications including testing, monitoring and measuring. The programming interface of LabVIEW is graphical and based on data flow along wires between functions. A LabVIEW file consists of two parts. One is a block diagram containing the executable code, while the front panel is a graphical interface consisting of controllers, indicators and instructions shown to the user. Thus, the end user may never have to see the code behind the actions.

Figure 5.1 shows an example of a block diagram code. The piece of program shown is used for changing the angle of the QWP. The parameters on the left are given as an input for this piece, and the output parameters are shown on the right. In the first column of the so-called sequence structure, the QWP motor is told to start moving towards the desired QWP angle. In the second column, the program continuously checks if the motor is still moving or not. When the motor stops, the delay set by the user is awaited before measuring the final angle.

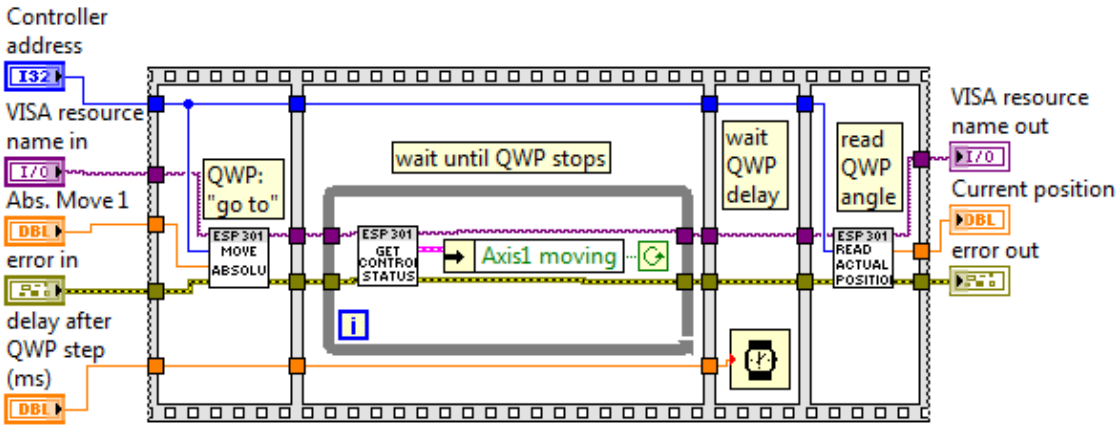

Figure 5.1. *Example of a block diagram of a LabVIEW program.*

The devices controlled by the microscopy control program produced in this Thesis are the motor of the QWP, the nanopositioning stage and the photon counting system. The program is based on the original LabVIEW interface of the nanopositioning stage, made by Mad City Labs. The interface was, however, modified significantly for matching our purposes. The original program was designed only for moving the stage and reading its actual positions. For us, the stage movement is of course an important detail, but, for example, the reading of the actual positions is mainly only a tool for troubleshooting and not in active use. On the other hand, the control properties of the QWP motor and the photon counting devices are equally important as the stage movement control and thus they were included in the program. The control of the laser is excluded from this user interface and has to be done manually via a laser control unit. This choice was made because in our measurements the laser beam should be very stable and thus it is better to let the laser be without any additional external control. However, synchronization of the microscopy system with wavelength sweeping of the laser can be considered for specific use in the future.

Connection and communication between LabVIEW and the instruments is performed through dynamic-link libraries (DLLs) delivered with the instruments. As mentioned earlier, all instruments have their own sample LabVIEW user interfaces including the most common actions with that device. These codes illustrate how the computer can be connected to the device, what kinds of preparations have to be made before the instrument can be used for proper measurements, and what kinds of actions one can execute. By utilizing these sample codes and functions included in the DLLs, the microscopy measurement sequence was designed and the program for executing it was built.

5.2 Measurement algorithm

The parameters defining the details of the measurement are given by the user in the front panel of the program as described in detail in the next Section. In this Section, the

main focus is the logic of the measurement algorithm. The main idea in the polarization-resolved nonlinear scanning microscopy is that the sample is illuminated with a focused laser beam with a certain polarization and the intensity of the nonlinear signal is measured along the sample area pixel by pixel. The algorithm for implementing such a measurement is shown in Figure 5.2. The user can adjust the details of the measurement, but the logic of the execution during the measurement is always the same. First of all, the program defines the scanning route along the sample area by using parameters the user has given.

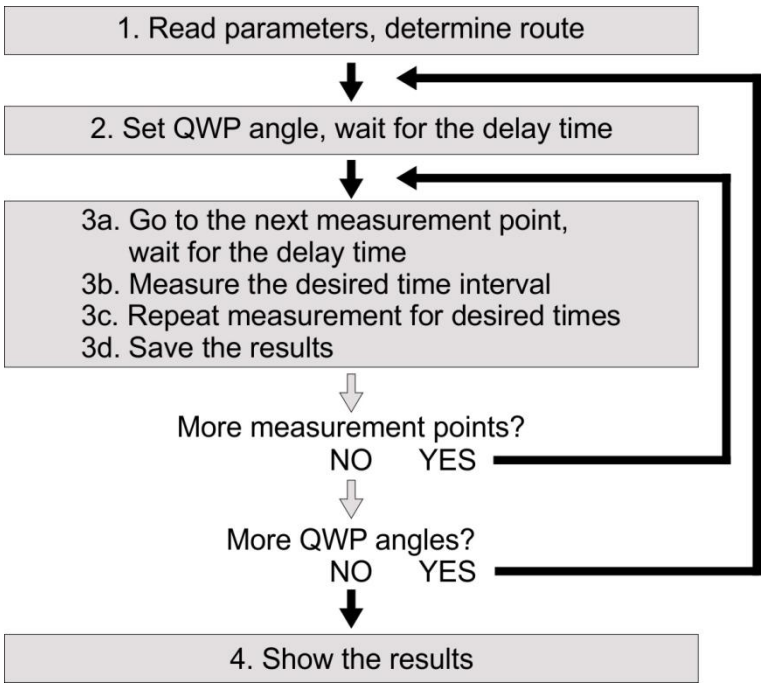

Figure 5.2. *Measurement algorithm of the microscopy program.*

Before starting the scanning process, the QWP has to be set to a certain angle to achieve the desired initial polarization state of the input beam. Whenever the QWP or the scanning stage is moved, there is a delay before the next action to ensure that the system reaches stability. When the QWP angle is the desired one, the scanning process can be started. After the scanning stage has reached the first measurement point and the delay has expired, the PMTs are activated for measuring the signal from the sample. Photons are collected for the time defined by the user, and the measurement is repeated immediately again if averaging over many measurements is desired. After saving the photon counts to the memory of the program, the stage is moved to the next scanning point and the signal collection is repeated.

When the last measurement point is reached and the photon measurement there completed, the program checks if there are still desired polarization states of the excitation beam left. If this is the case, the whole scanning is repeated with another QWP an-

gle. When the measurements are completely finished, the results are shown to the user and can be exported for later use.

5.3 Parameters for adjusting the scan

As mentioned earlier, the program consists of the block diagram and the front panel. The end user is working only with the front panel, and in this Section the parameters that can be set there are introduced. The figure of the whole front panel is shown in Appendix 2 and some parts of it are presented more closely in Figures 5.3-5.7. The design of the front panel has been made as easy and logical to use as possible, even for a new microscopy user.

When the program is started, it connects automatically to all the required devices. If an error occurs during the connection, the user is informed. Otherwise, after starting the program, the settings for the scan can be immediately given. The most important settings for microscopy scanning are to determine the scanning area and resolution, for how long the signal is collected for each data point, and which input polarizations are used.

Scanning area. As the nanopositioning stage is able to move in three dimensions, the direction of the plane where the scanning is done can be chosen from three options. This means that the user can determine if the scan is done in the *xy*-, *xz*-, or *yz*-plane. Usually the scan is performed in the *xy*-plane, whose normal is parallel to the beam propagation axis, as that is the plane of the sample plate and as the resolution and the moving range are better for the *x*- and *y*-axes than for the *z*-axis. Once the scan plane is set, the other scanning area options are given. The selector for setting the scan plane is shown in Figure 5.3.

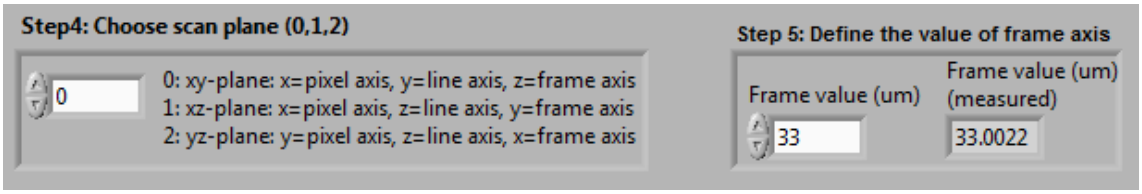

Figure 5.3. *The selectors for setting the scan plane and frame axis value and the indicator showing the current value of the frame axis.*

There are two different possibilities for the type of scanning: raster scanning or random scanning route. In raster scanning, the scanning area is a rectangle which is scanned pixel by pixel. In the random scanning route the user can set the route in the measurement area freely, and the scanning is done by following that path. The route is determined by a text file containing, when *xy*-scan is used, the *xy*-coordinates of all the points of the route. Also, the maximum distance between the measurement points is set. Then the program calculates the measurement locations according to this information. The random route setting is not used in normal microscopy scans, but is also included in

the program for possible future needs, such as arbitrary scanning purposes, e.g., lithography, targeted photobleaching or optical trapping.

For raster scanning, the naming of the axes is as follows: the axis perpendicular to the scan plane is called the frame axis and the two others are the pixel axis and the line axis. During the scan the sample is moved so that the line axis value remains the same until all points in the pixel axis are scanned once. The user can choose if the points in the pixel axis are always scanned from small to large values, or every second time from large to small values. This option is called snake scanning and it minimizes the movement of the stage.

The value of the frame axis stays constant during the scan. However, it can be adjusted before the scan. This makes 3D-scanning possible as the same area can be measured for different well-defined depths. The possibility to fine-tune the frame axis value interactively is also very useful while placing the sample surface to the focal plane of the focusing lens. The controller for changing the frame axis value is shown in Figure 5.3. Also, the positions of the two other axes can be adjusted in real-time when there is no ongoing scan.

When the raster scanning option is used, the starting and end positions of the scan region have to be set separately for the pixel and the line axes. The values are in micrometres and relative to one corner of the moving range of the nanopositioning stage. The resolution of the scan is set differently for pixel and line axes. Here, the resolution means the number of measurement points in each axis. Thus, if one wants to measure at pixel axis points 0, 1, 2 and 3, the starting value at pixel axis should be 0, end value 3 and resolution is set to be 4.

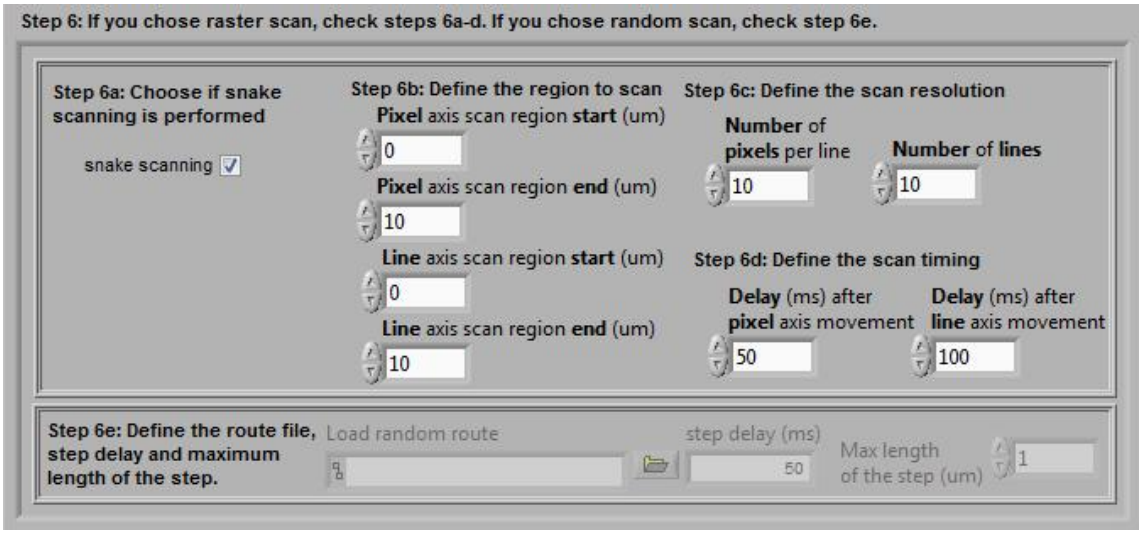

Figure 5.4. *The front panel settings for the scanning area, the resolution and the delays after moving the axes. The abbreviation 'um' stands for micrometer and is relative to one corner of the scanning area.*

Other important parameters are the delays after the axis movement before starting the intensity measurement. They are set differently for the pixel and the line axes. The

default values are 50 ms delay for the pixel axis and 100 ms for the line axis. If the scan is done with the random route setting, the delay is the same for both axes as there is not any raster pattern done, instead the route is arbitrary and in that sense both axes in the scan plane are equivalent. The delays should be chosen carefully. Too short delays produce shifts from the wanted measurement locations and too long delays cause scans to take an unnecessary long time. Figure 5.4 shows the part of the front panel in which the scanning area and axis settings are chosen.

Photon counting settings. The microscopic images are formed by measuring the nonlinear signal intensities for each pixel. For that purpose, the photon flux with a certain wavelength emitted from the sample is detected. For getting reliable results, averaging over many measurements may be necessary at some situations. Thus, the number of photon collection measurements at each measurement location can be chosen. Also the length of the time interval for photon counting in each measurement has to be set. The values are given in milliseconds and the default value is 50 ms.

The photon counting system has two channels, A and B, which can be used either separately or at the same time. For example, the SHG signal can be measured both from reflection and transmission modes. Another possibility, as done in the measurements in this Thesis, is to collect the SHG and THG signals at the same time from the reflected signal. The controllers for setting the photon collection parameters are shown in Figure 5.5.

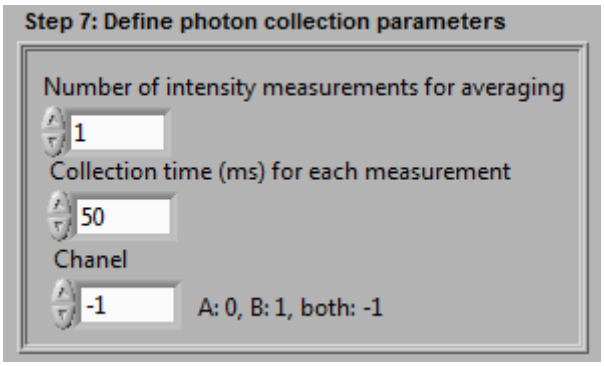

Figure 5.5. *The controllers for setting the photon counting parameters.*

Polarization settings. The polarization of the input field is adjusted with the QWP located right before the focusing lens of the microscope. Within a single program run, the scan can be done with only one or with many different QWP angles. If many angles are used, they have to be at constant intervals. The delay before the start of the scan after the QWP movement can be set, and its default value is 500 ms. This delay is quite long, but does not affect the total duration of the run significantly as the QWP angle is usually changed only a few times during one measurement sequence. A part of the front panel for the QWP parameter settings is presented in Figure 5.6. The QWP angle can also be programmatically changed in real time, not only just before the scan or during a run. It is also worth noting that the implemented polarization control here is not restricted to

QWP use but can be applied for other desired waveplates or polarizers mounted on a motorized mount that can be connected to the controller.

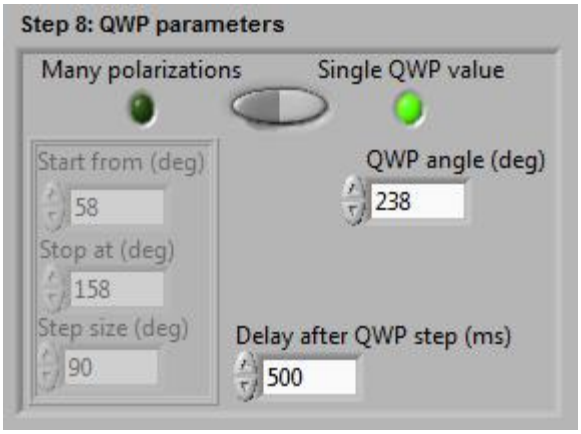

Figure 5.6. *The controllers for the polarization settings.*

Information shown to the user. The program always shows the expected total time for the scan if it would be done with the selected parameters. Thus, the user can adjust, for example, the resolution, the number of intensity measurements at each location, the photon collection time, or the delays for seeking a reasonable run time. When the scan is started, the start time and the expected end time of the scan are shown. The ongoing scan can be aborted with the StopScan-button. These and the button for starting the scan are shown in Figure 5.7a).

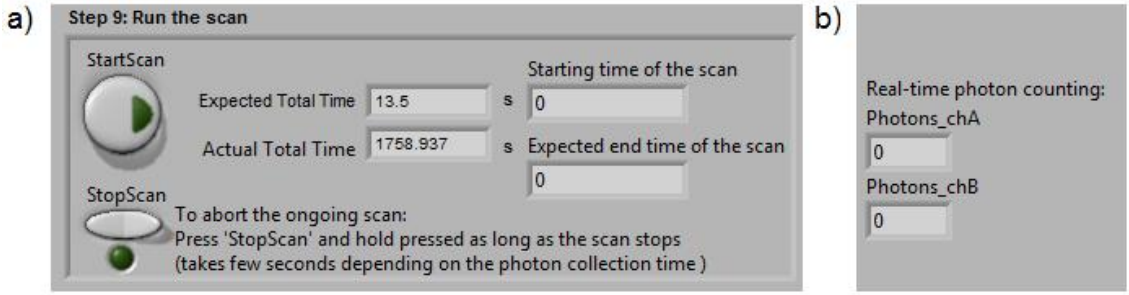

Figure 5.7. *a) The buttons for starting and aborting the measurement sequence and displays for showing the duration information for a user. b) The displays for showing the real-time information about the photon signals in channels A and B.*

Before starting the scan, the user has to remember to enable the photon counting detectors and open the laser shutter. Both of these have to be done manually outside the program. If the photon signal is zero upon starting the scan the program shows a warning. However, when the detectors are enabled there is always a small noise signal, and thus the warning is not necessarily shown even if the laser shutter is closed. Thus, before pressing the start button it is a good convention to check from the real-time photon counting displays, shown in Figure 5.7b), if there is a reasonable signal or not. These displays show the signal levels also during the ongoing measurement.

Presenting and saving the results. When a measurement run is finished, the results are shown as raster intensity patterns for both channels. The results for one QWP angle are shown at a time, and there is a selector for changing the display for results with different polarizations. Unfortunately, this option of showing intensity results is not available if the scan type is random route scanning, as its implementation with LabVIEW features would have been extremely complicated. Furthermore, although real time display of signals can be done in principle, we chose to display the results after the run due to time and memory issues.

The intensity results can be saved in five different kinds of formats, one of which is a picture and four are text files. When saving the results, an "info" file is also saved. It contains the description of the measurement settings in the form shown in Figure 5.8, as well as short instructions of how to read the result file. The examples of the results file contents, corresponding to the measurements introduced in Figure 5.8, can be found in Appendix 3 with their instructions saved in the beginning of the info files. There, one example file content is shown for each result saving type.

```
Number of intensity measurements for averaging:
3
Collection time for each measurement(ms):
50
Chanel (A:0, B:1, both: -1):
-1
Delay after QWP step(ms):
500
Raster or random route scan:
raster
Pixel axis: x    Line axis: y    Frame axis: z
Width of the scan region in pixel direction(um):
3
Width of the scan region in line direction(um):
3
Number of pixels:
3
Number of lines:
3
Delay after pixel axis movement(ms):
50
Delay after line axis movement(ms):
100
Snake scanning:
no
Frame value(um):
33
```

Figure 5.8. *Example of how the used measurement settings are saved in a text file whenever results are exported.*

The picture option saves the intensity raster figures. That intensity raster can also be saved in a numerical form to a text file. The number of these files equals the number of

used QWP angles. Another option is to extract only the total intensities in the measurements, meaning the sum of the photon counts over all pixels, for each QWP angle. This can be done so that, for every measurement time, either its own total intensity or only the total intensity average over all measurements is calculated and saved. In these cases only one file containing the total intensities for all used QWP angles is saved. And of course, the intensity results can be extracted just as they are measured, meaning that all measured intensity values at each measurement location are saved without summing or averaging them. In this case the number of converted files is the number of used QWP angles times the number of intensity measurements for averaging at each measurement location. In all cases, if two measurement channels are used the number of files is doubled when compared to a measurement with only one channel. In addition to the intensity results, the realized location data during the scan can also be extracted.

6. MEASUREMENTS

6.1 Test samples

For testing the basic capabilities of the developed nonlinear optical microscope and especially its extensive functionalities which can be accessed via the user interface created, nonlinear imaging of metal nanoparticles was done. The test samples were CPM samples, which were fabricated by Dr. Israel De Leon (Department of Physics and School of Electrical Engineering and Computer Science, University of Ottawa, Ottawa, Canada) and investigated in ref. [47] with linear CD spectroscopy and SHG microscopy. Aside from verifying the SHG measurements from such nanostructures, we also extended the measurements to THG and consequentially, nonlinear CD microscopies to determine if the overall sample geometry and corresponding optical quality can be probed also using these novel imaging contrast mechanisms. All the measurements were done by using the raster scan option of the scanning program and under circularly-polarized beam excitation unless otherwise stated.

The CPM samples were fabricated with electron-beam lithography and consisted of three arrays consisting of differently shaped gold nanoparticles: right- (RH) and left-handed (LH) gammadions as well as cross-shaped nanoparticles. All of these structures have a line width of 80 nm and a side length of 400 nm as illustrated in Figure 6.1. The gold layer is 100 nm thick and located on top of a 5 nm adhesion layer of titanium deposited on a borosilicate glass substrate. Shown in Figure 6.1 is a schematic of a RH-CPM sample and its sample environment. All samples were arranged in a square array with a particle-to-particle period of 800 nm as shown in Figure 6.2, which shows a representative portion of the arrays consisting of crosses and LH- and RH-shaped CPM samples. Cross samples are achiral, while gammadion samples are chiral. The effect of nanoparticle chirality is anticipated during the nonlinear microscopy measurements.

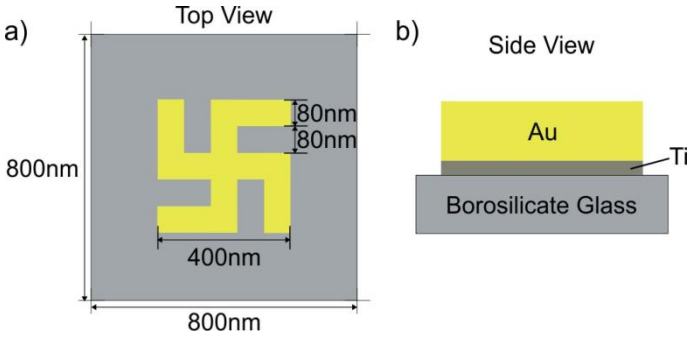

Figure 6.1. *Schematic diagram of the unit cell of the RH-CPM sample as viewed from the top (a) and side (b). [52]*

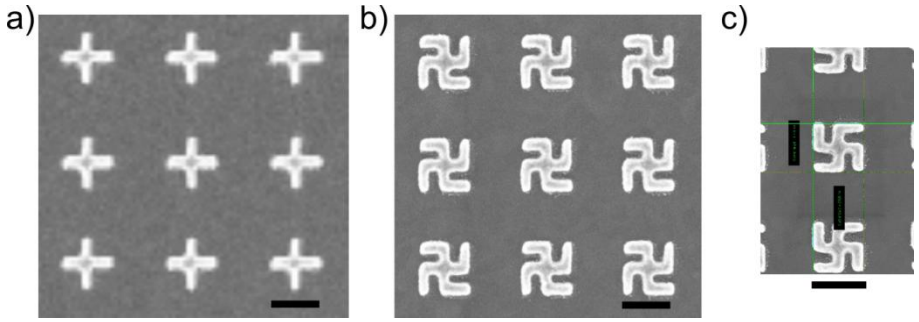

Figure 6.2. *Scanning electron micrographs (SEM) of the array of gold nanostructures consisting of cross (a), LH (b) and RH (c) shaped CPM samples. Scale bar = 400 nm. Data were provided by Dr. Israel De Leon.*

The typical transmittance spectra curves of the RH-CPM sample are shown in Figure 6.3. There the excitation is done with RHCP and LHCP light, which were used in our microscopy measurements, too. Mostly, the absorbance is almost the same for both polarizations, but in the visible light region between 600 and 800 nm there is a significant difference making CD measurements possible. This can be utilized when UV-VIS CD spectroscopy is made, as demonstrated in ref. [47]. In our experiments, however, the fundamental excitation wavelength is between 1040 nm and 1070 nm. Thus, the SHG and THG wavelengths are at around 520 to 535 nm and 347 to 357 nm, respectively. Based on Figure 6.3 it can be seen that for the fundamental wavelength there is almost minimal absorbance for both circular polarizations. For the SHG wavelength the absorbance is significantly higher, but the transmittance is still over 50 %.

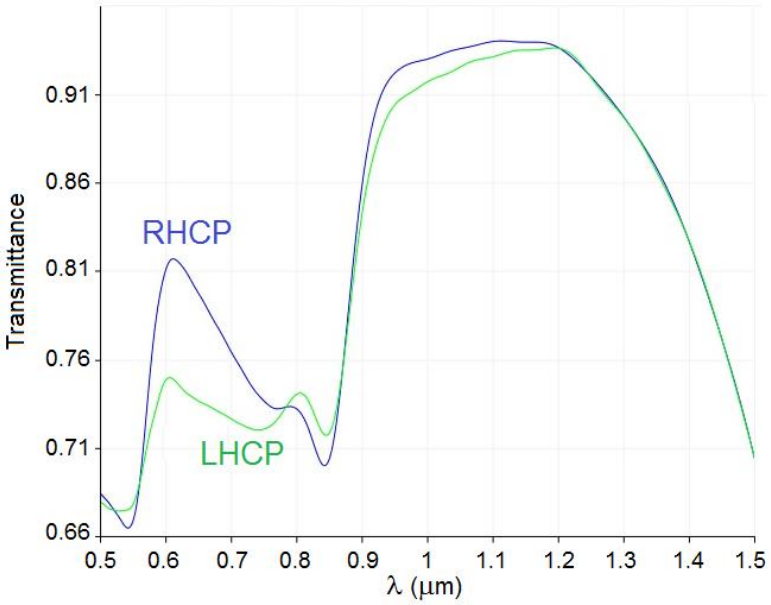

Figure 6.3. *Transmittance spectra of the RH-CPM sample for RHCP and LHCP light (Data were provided by Dr. Israel De Leon).*

6.2 Sample positioning

Prior to sample scanning, it is necessary to inspect if the beam focus impinges the sample at the correct position. Thus, the transverse position of the sample with respect to the beam position was verified with a brightfield imaging arm of the microscope consisting of a white light source, a condenser and a CMOS camera. The setup was made in a way that only by adding a flip mirror to the setup and switching on a light source, the camera can be used. Then, by switching the light source off and removing the mirror, the setup can be easily returned to nonlinear microscopy operation.

To adjust the position of the samples along the transverse position of the focal plane, two manual micropositioners which move the stage along the *x*- and *y*-axes were used while monitoring the movement with the camera. To adjust the axial position of the samples relative to the focal point, a manual micropositioner which moves the sample along the *z*-axis was used. Here, the sample positioning was achieved upon observing the sharpest possible image of the sample on a computer screen.

For fine tuning of the sample location in the *z*-direction, the real time photon counting feature of the microscopy program was used. The sample position was changed by the frame axis value controller and the focus was searched by checking when the nonlinear signal is the highest. For demonstrating how the sample positioning in the *z*-direction affects to the nonlinear signal, Figure 6.4 show the total SHG and THG intensities for raster scans made with different *z*-values, while otherwise keeping the settings unchanged. The sample was RH-CPM and RHCP light was used for excitation.

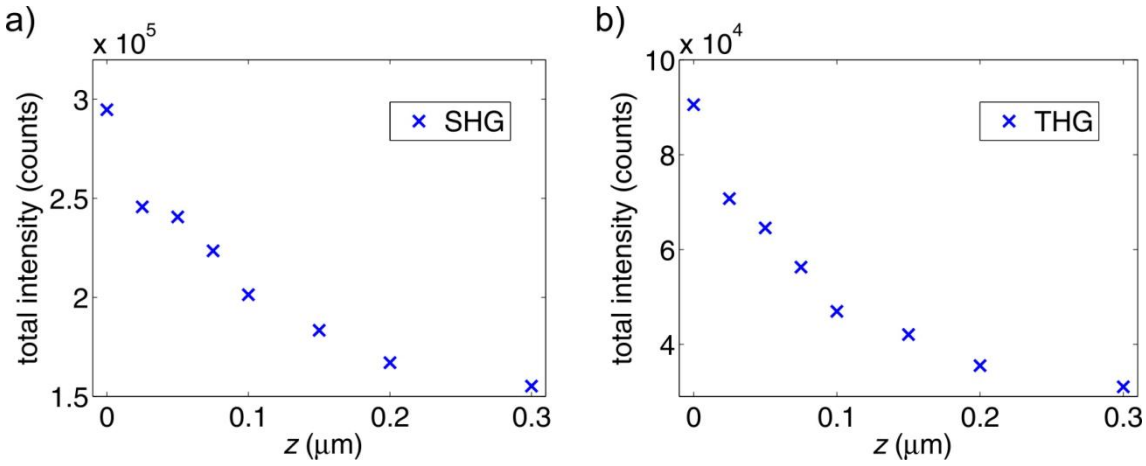

Figure 6.4. *Measured SHG (a) and THG (b) intensities decrease drastically when the RH-CPM sample's position in z-direction is changed away from the focus, which is located at the position z = 0.*

As expected from coherent NLO processes, the dependence of the nonlinear signal on the relative position of the sample surface with respect to the incident beam's focus is very strong (Figure 6.4). This is why it is important to adjust the sample surface carefully to the focus as otherwise the signal levels would be low producing images with poor contrast. We also noticed that whenever the measurement location within one

sample or set of samples were changed, the *z*-position had to be optimized separately. This can be associated with an uneven sample surface or possible drift of the sample in the *z*-direction relative to the stage.

6.3 Parameter tests

One aim of these measurements was to demonstrate how the values of different parameters in the program affect the results. This was made by changing the scanning parameters one at a time and repeating otherwise the same raster scanning measurement many times. The used sample was RH-CPM and the excitation was made with RHCP light. The scans were made in the *xy*-plane and the delay after the pixel and the line axis movements were 50 ms and 100 ms, respectively. The 'snake scanning' -option was not used. If not otherwise mentioned, the basic settings used in the measurements expressed both in this and the following sections were: scanning area of 6 μm × 6 μm, resolution of 50 pixels in both directions, photons were collected for 50 ms and averaging over 3 measurements was done. The fundamental beam had the wavelength of 1060 nm and both the SHG and THG signals were collected in the reflection mode, as in all the measurements presented in this Thesis.

Scanning area. First, the SHG and THG signals from a region of the RH sample were measured by varying the effective scanning area. The resolution, meaning the number of pixels per scan axis, was kept at constant 100 × 100 pixels and the photons were collected over 100 ms and only one measurement was made at each pixel. The intensity patterns with three different scanning areas are shown in Figure 6.5. Common to all these images is the observation of hotspots that form a regular pattern which corresponds well to the expected arrangement of the nanoparticles in the array. However, all the particles do not behave equally, i.e., there is strong variability in the overall signal level detected from each nanoparticle. As an example, there are some points exhibiting much stronger signals than could be expected to occur, suggesting the presence of sample imperfections. These can be caused, for instance, by problems in sample fabrication or preparation, contamination or laser-induced damage.

A remarkable fact is that the same imperfections are mostly seen in both the SHG and THG images. With these features one can see that the scanning area is every time enlarged so that the lower left corner in each subfigure is at the same location in the sample plate, verifying the high controllability of the scanning system. Thus, the darker rectangle in the lower left corner of the pattern in Figures 6.5c),f) is probably because of the fact that this area was exposed with laser already in the earlier measurements and thus some sample burning has occurred resulting in the lower signal levels.

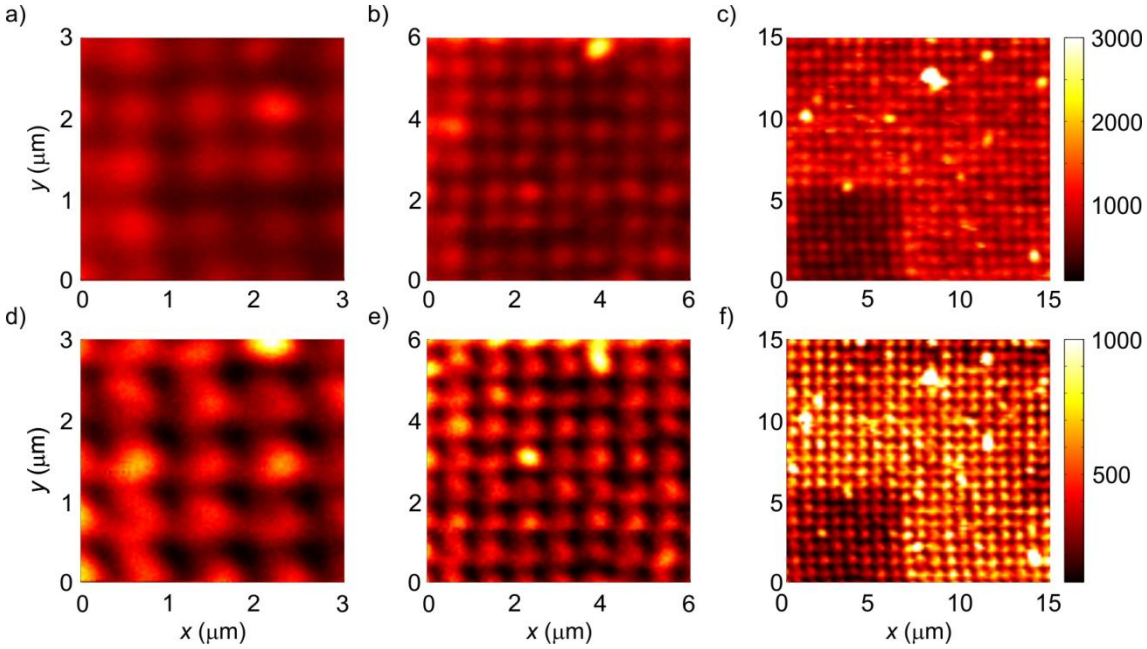

Figure 6.5. *SHG (a-c) and THG (d-f) signals from RH sample with three different scanning areas. The colour bars are valid for all the figures in the same row.*

Pixel resolution. Next, we examined the effect of the pixel resolution to the acquired SHG and THG images of the samples. Figures 6.6a)-d) and 6.6e)-h) show the SHG and THG signals, respectively, measured from the same part of the sample pattern with different pixel resolutions. In Figures 6.6a),e), there is no clear regular hot spot pattern. In Figures 6.6b),f), an observable regular pattern starts to be visible, but the individual hot spots are still hard to distinguish. However, in Figures 6.6c),g), the hot spots are clearly separated from each other.

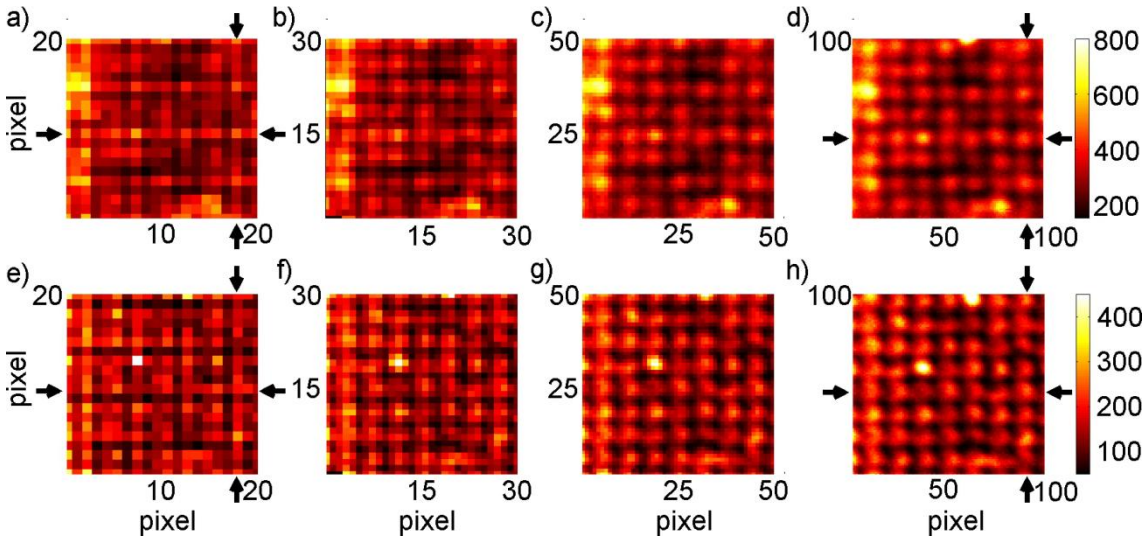

Figure 6.6. *SHG (a-d) and THG (e-h) signals of the same scanning area at four different resolutions. The colour bars are valid for all the figures in the same row. The arrows represent the lines along which the intensity profiles of Figure 6.7 are taken.*

Between Figures 6.6c),g) and 6.6d),h) the resolutions doubles, but the quality of the image is not remarkably improved. Thus, it is important to figure out what is the reasonable resolution when large sets of measurements are done, as its value has a huge impact on the duration of the scan. Here, the pixel resolution is conveniently defined as a number of measurement points in a raster pattern direction and not determined in micrometers. Thus, in order to maintain a reasonable image quality for different scanning areas, one has to change the pixel resolutions accordingly.

For a more detailed analysis of the spatial resolutions achieved along the transverse directions, we plotted the measured intensity values as a function of position in Figure 6.7. This analysis is made only for measurements with the lowest and the highest resolutions, and the lines along which the profiles are taken, are indicated with arrows in Figure 6.6. The intensity peaks caused by hot spots can be clearly distinguished in Figure 6.7 and the intensity patterns are almost similar with both resolutions. Thus, even if it is quite difficult to observe any clear regular hot spot pattern from Figures 6.6a),e), the regularity can be seen when the intensity pattern along the hot spot line is made.

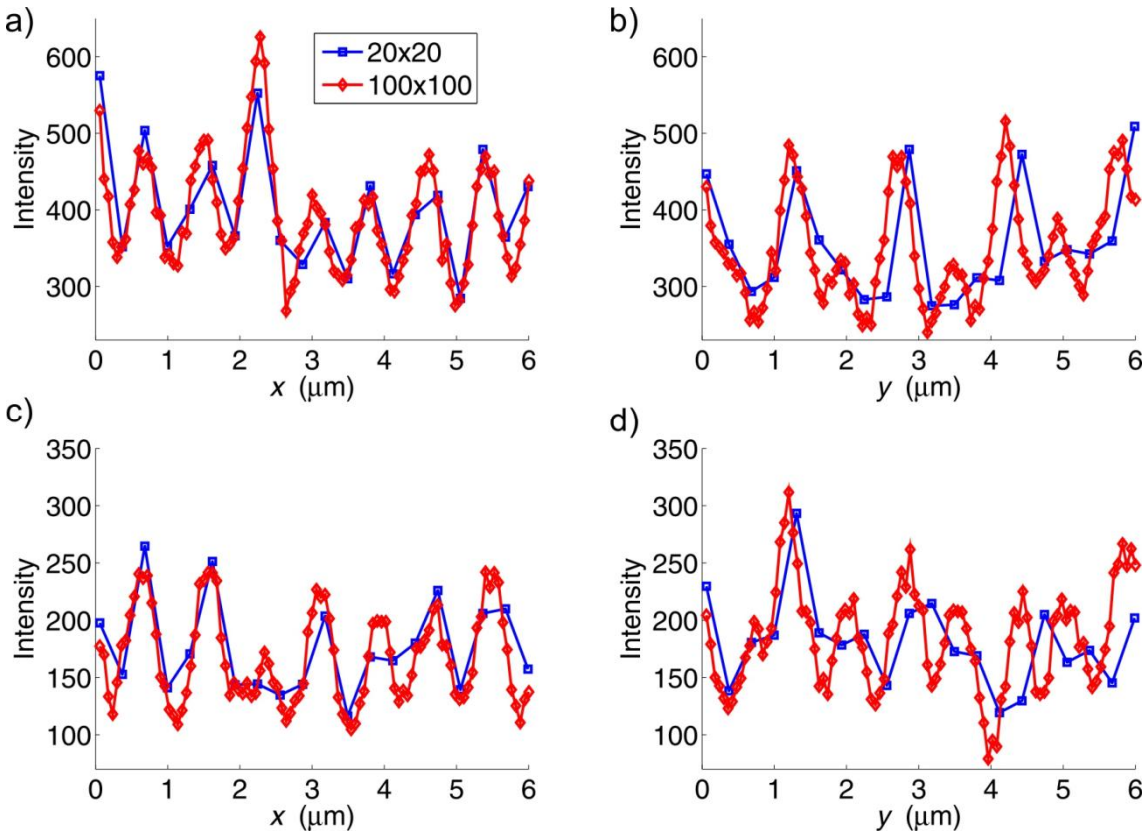

Figure 6.7. *Intensity profiles along one pixel chain in the SHG (a,b) and THG (c,d) images shown in Figure 6.6. Profiles a) and c) are along the horizontal direction and b),d) along the vertical direction in Figure 6.6. Square (diamond) markers are for measurement with the resolution of 20×20 (100×100).*

Furthermore, from Figure 6.7 the full width at half maximum (FWHM) of the hot spot peaks can be calculated. For this purpose, the base line of the signal has to be set, and it is estimated to be at the intensity value of 150 (60) for SHG (THG). Then, the FWHM was calculated for the measurements with the resolution 100×100 pixels. In total, 5 different hot spots are used for determining the FWHM values, and not all the used peaks are shown in Figure 6.7.

As a result, the FWHM of the hot spots can be said to be about 600 nm for SHG and 500 nm for THG with a fundamental beam spot size of 800 nm. As THG is a higher-order process, the spot size should be smaller for it, as it was. These values are a bit larger than the size of one sample particle, and the gap between the particles, which both were 400 nm. Thus, we cannot really separate individual particles and there probably is some coupling between them, producing a different kind of signal compared to the signal expected from one individual particle. This has to be taken into account when judging the results presented in this Thesis.

Photon counting settings. The dependence between the total intensity of the nonlinear signals over the scanning area and the photon collection time was also investigated and the results are shown in Figure 6.8a). The assumption is that the longer the nonlinear signal is collected, the larger is the intensity. In fact, as long as coherent NLO signals are generated and they remain as the dominant process throughout the exposure time, the dependence should be linear. When linear fits are made to the data sets shown in Figure 6.8a), the R^2-values are 0.9999 and 0.9997 for SHG and THG, respectively. As these values are really close to one, it is verified that in practise the total nonlinear intensity is linearly proportional to the photon collection time.

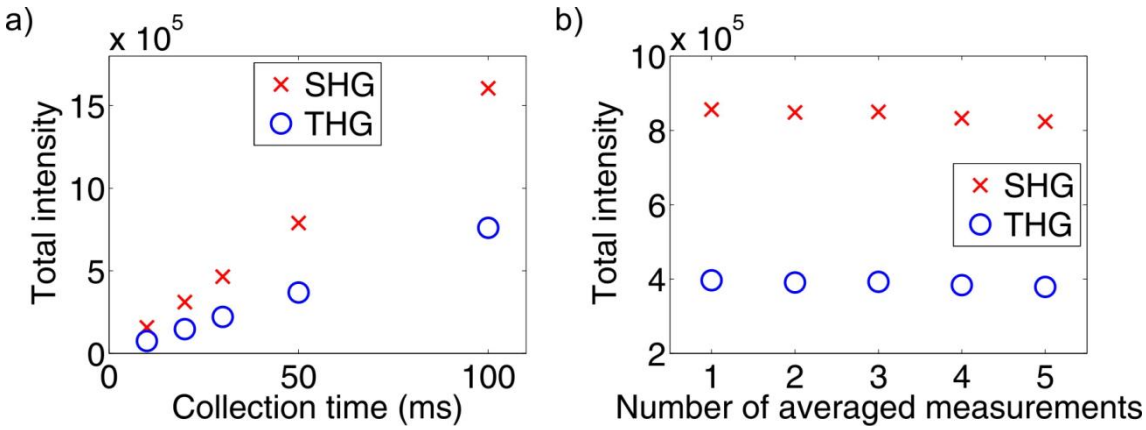

Figure 6.8. *Effects of the increasing signal collection time (a) and number of measurements for averaging (b) in the detected SHG and THG signals.*

As mentioned earlier, the number of intensity measurements in every pixel can be adjusted in our microscope. This means that the same measurement is repeated many times in the same location relative to the sample, and finally the average of these results

is expressed as an intensity value for that pixel. In principle, if the signal collection time is kept constant, but the number of measurements in each measurement point is changed and always an average of the results in that point are taken, the total intensity over the whole sample area should be constant. The results of this kind of experiment are shown in Figure 6.8b) for SHG and THG.

As seen from Figure 6.8b), the total intensity of the SHG and THG signals seems to stay almost constant while the number of averaged measurements is changed. However, the intensity is slightly decreasing with increasing number of measurements. This may be because of possible sample burning as all the measurements were repeated right after each other. However, based on this it can be said that for this sample there is no reason for using more than one measurement for averaging, as the increased number does not improve the results. As the situation can be different for different materials, it is worth testing this parameter whenever a new kind of a sample is measured in order to achieve reproducible results within reasonable schedules.

6.4 Verification of second- and third-harmonic signals

As has been mentioned a few times already, usually a pulsed laser is needed for the observation of NLO effects, as the required intense electric fields cannot be produced with the excitation by a continuous-wave (CW) beam. Here, this is verified by measuring the SHG and THG intensities with excitation by CW laser light. This was done by turning off the mode-locking operation of the Chameleon laser using the “alignment mode”.

First, the normal measurements were made, and the results, shown in Figure 6.9a),b), correspond to the previous measurements introduced in Section 6.3. However, when the laser is changed to CW operation of the same average power, the signals drop to below one tenth of the original levels and not any regular pattern is seen (Figure 6.9c),d)). The conclusion of the Figure 6.9 is that the SHG and THG processes with these kinds of samples are not driven by the CW laser source, but only noise can be detected when illumination is made with the CW beam.

As can be seen from Figures 6.9c),d), the noise is higher for the SHG than for the THG channel. The difference between the noise levels can be mostly explained with the fact that our SHG signal has the wavelength of 530 nm, located in the visible spectral region. Thus, a significant portion of the noise detected with the SHG channel probably is because of light leaking from the light sources in the laboratory room, such as computer screen used for monitoring the measurement. The SHG noise can be further minimized by isolating the measurement system better from external light sources, meaning that instead of a black curtain, for example, a tighter box could be used. Furthermore, as can be seen from Figure 6.9a),b), and has already been seen in Section 6.3, the SHG signal is stronger than the corresponding THG signal. It is because SHG is, in general, and for our samples as well, a more efficient process than THG.

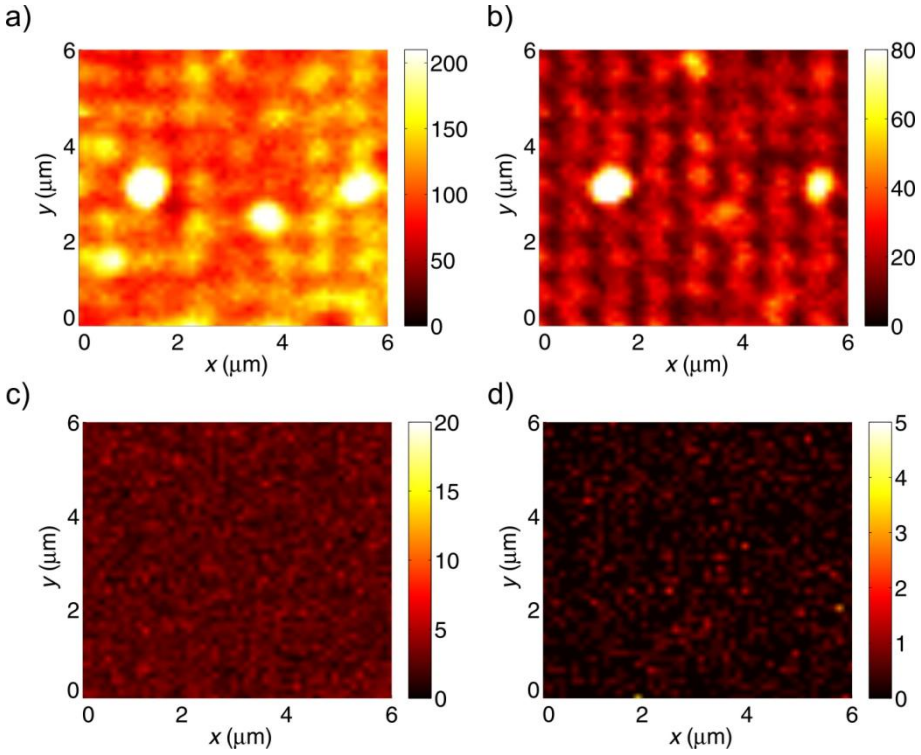

Figure 6.9. *SHG and THG signals from the RH-CPM sample when the excitation is made with pulsed (a,b) and CW (c,d) laser beam.*

As already mentioned in Section 4.5, the separation of the SHG and THG signals from the fundamental one and from each other is carried out with appropriate optical filters. For ensuring that the detected signals really are SHG and THG signals, we repeated the same measurement while changing filters between the scans. Once again, the sample was RH-CPM and RHCP light was used. The excitation wavelength was 1060 nm and kept constant during the measurements. Thus, the SHG and THG wavelengths were 530 nm and 353 nm, respectively. Figure 6.10 shows the relation of the wavelength ranges of the filters in the SHG arm with respect to the fundamental, THG and SHG wavelengths. Filters ii and v are the original filters, used for blocking the fundamental and THG light reaching the SHG detector.

By keeping filter v in its place but changing filter ii to some other with the transmission range near that of filter ii, we can observe if there is a significant signal level outside the SHG region or not. This experiment was made with three different filters, marked as i, iii and iv in Figure 6.10. The corresponding intensity images are also shown in Figure 6.10 and the total intensities of these figures are calculated in Table 1. When the original filters are used the signal level is significantly higher compared to the other situations, and that is also the only case when a clear regular hot spot pattern can be seen, although there seems to be some weak signal from the sample at other wavelengths, too.

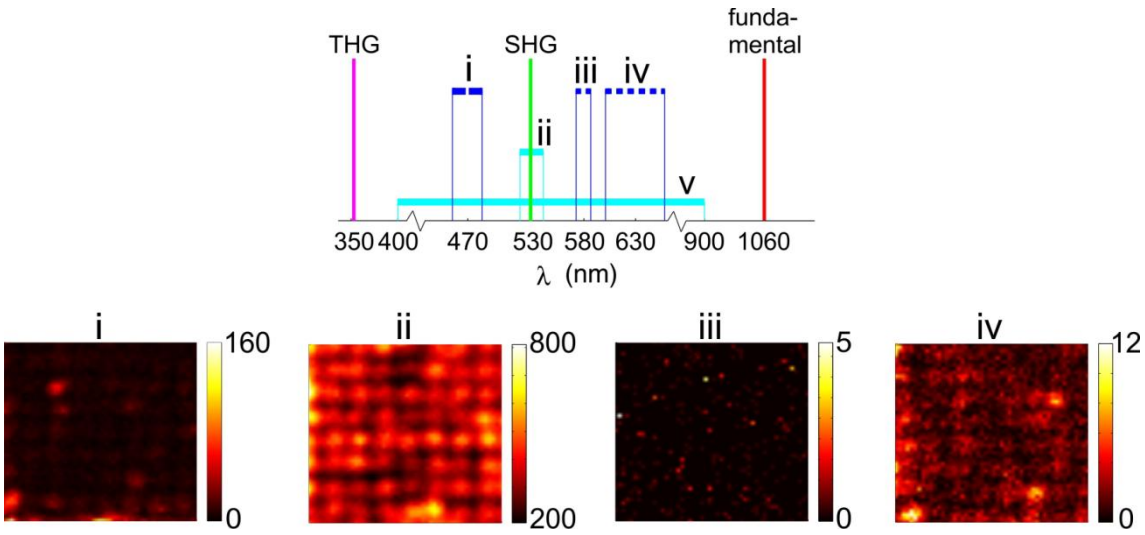

Figure 6.10. *Wavelength ranges of used filters in the SHG arm and the intensity patterns observed with different filters.*

Table 1. *SHG intensity with different filters in the SHG detection arm. The excitation beam had a wavelength of 1060 nm.*

Filter	Central wavelength of the filter (nm)	SHG intensity ($\times 10^4$ counts)
i	470	3
ii	531 (original)	90
iii	580	<1
iv	629	<1

These kinds of experiments were made for the THG channel, too. There the first filter, marked as iv in Figure 6.11 and Table 2, enables both the SHG and THG light to pass it. On the other hand, the second filter, marked as ii, alone would let both the THG and fundamental light to pass as it has two band pass regions. But when these two filters are used together, only photons near the THG wavelength can reach the detector. For testing the origin of the signal in this channel the filter ii was replaced with two other filters, one at a time, and the results are shown in Figure 6.11 and Table 2. Again, the only clear hot spot pattern and significantly higher total intensity was reached with the original arrangement. Thus, we can say that there is no significant signal with frequencies surrounding the SHG and THG frequencies, suggesting that the signals we observe are indeed originating from the SHG and THG phenomena. The specifications of the used filters are shown in Appendix 1.

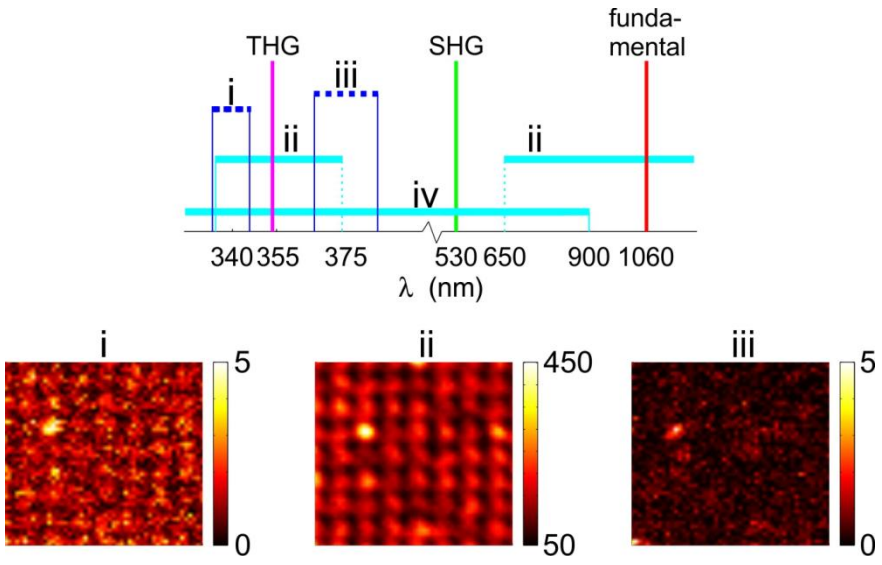

Figure 6.11. *Wavelength ranges of used filters in the THG arm and the intensity patterns measured with different filters.*

Table 2. *THG intensity with different filters in the THG detection arm. The excitation beam had a wavelength of 1060 nm.*

Filter	Central wavelength of the filter (nm)	THG intensity (×10^4 counts)
i	340	<1
ii	355 (original)	40
iii	376	<1

6.5 Power dependence of second- and third-harmonic signals

As explained in Chapter 2, the strength of the nonlinear signal is not linearly proportional to the strength of the excitation field, but the whole name nonlinear optics arises from the fact that this relation is nonlinear. On the other hand, we know that intensity is directly proportional to power. Thus, when intensity is marked as I, power is P and ω, 2ω and 3ω refers to fundamental, SHG and THG fields, respectively, we can state that

$$I_{2\omega} \propto P_{2\omega} \propto \left(P_{\omega}\right)^2 \tag{6.1}$$

and

$$I_{3\omega} \propto P_{3\omega} \propto \left(P_{\omega}\right)^3 . \tag{6.2}$$

The fulfilment of these conventions was investigated by measuring the SHG and THG intensities while the input power is varied.

Shown in Figures 6.12a) and 6.13a) are the power dependence curves of the SHG and THG signals detected from the LH-CPM sample under an arbitrary elliptical polarization. The measurement area was 5 μm × 5 μm, resolution 50 pixels, collection time 50 ms and the averaging was made over 5 measurements. Also a quadratic (third-order) fit function is shown for SHG (THG). The behaviour of the corresponding power dependence curve for SHG (THG) follows well the quadratic (third-order) assumption, but for higher powers the signal saturates. This can be because the detectors may not be capable of detecting very high signal levels. Thus, the last points after saturation are excluded from the data set for which the fits are made.

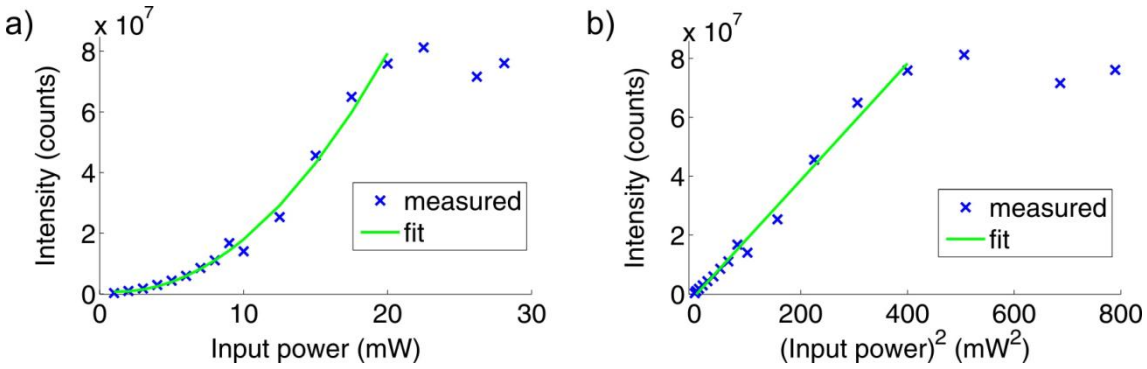

Figure 6.12. *Power dependence of SHG intensity, measured from LH-CPM sample.*

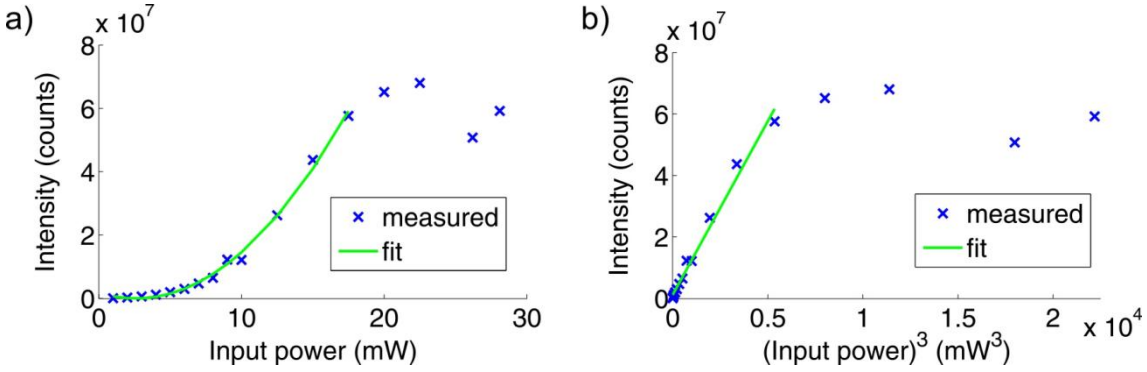

Figure 6.13. *Power dependence of THG intensity, measured from LH-CPM sample.*

Another way to examine the behaviour of the power dependence of nonlinear intensities is to plot them as functions of second (for SHG) and third (for THG) powers of the excitation power. This is shown in Figures 6.12b) and 6.13b). As expected, the observations are well in line, except the last, saturated, values. The R^2-values are 0.9887 and 0.9857 for SHG and THG fits, correspondingly. A perfect fit would lead to the value of 1, but the values we got are still compatible with the linear behaviour.

6.6 Second- and third harmonic circular dichroism

One important goal to implement with the CPM samples was the investigation of their responses to circular polarizations and thus their CD response. The goal was not to make any detailed analysis, but to roughly demonstrate how well the CD effect can be seen with these samples. The measurements were done with the wavelength of 1060 nm and the samples were cross-shaped and LH- and RH-CPMs. The measurement area was 8 μm × 8 μm and the resolution was 100 pixels in both directions. The SHG intensity patterns for these samples with the excitation with LHCP (RHCP) light can be seen in the first (second) column in Figure 6.14. The CD figures calculated from these two are shown in the third column in Figure 6.14.

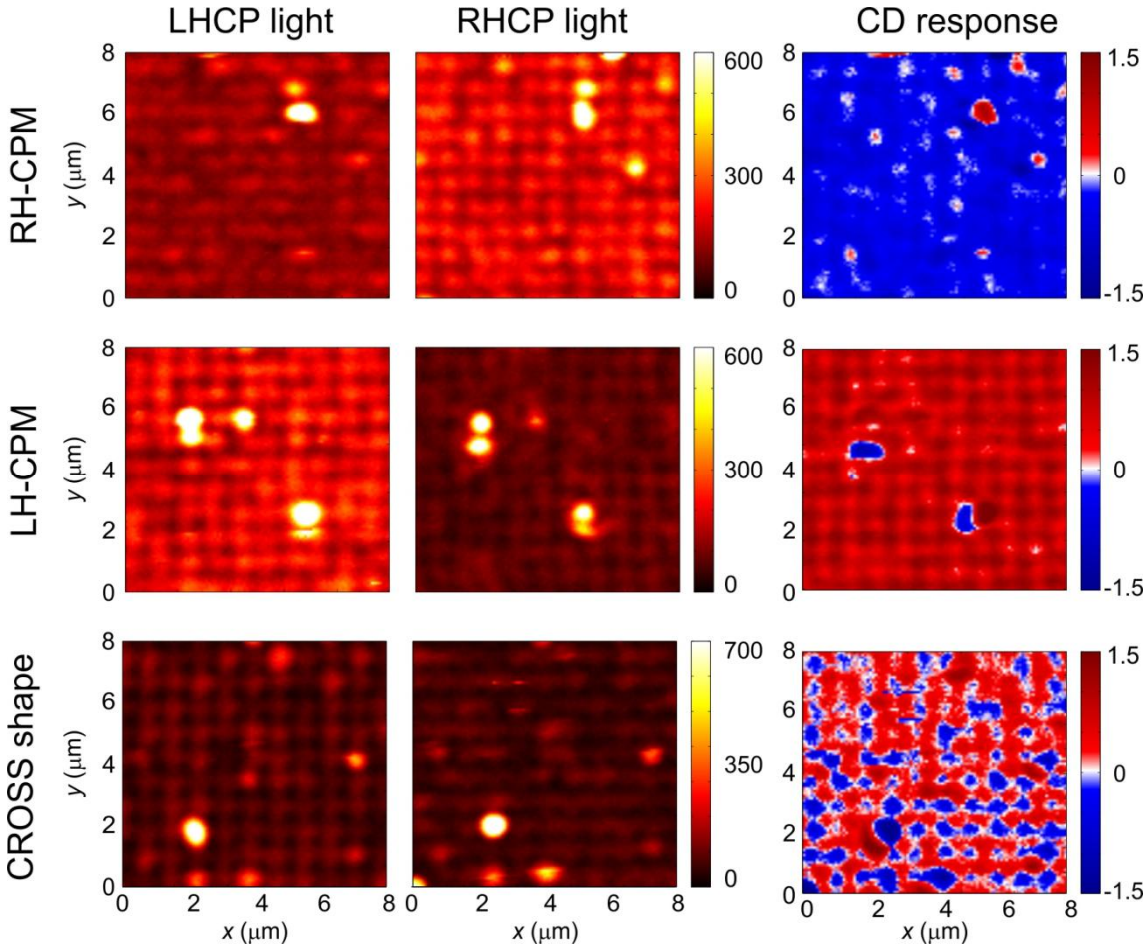

Figure 6.14. *SHG intensity patterns of two chiral (RH- and LH-CPM) and one achiral (cross) sample when the excitation was made with LHCP and RHCP light, and the corresponding CD responses.*

For chiral samples the SHG signal is stronger when the excitation is made with the light having the same-handed polarization than the handedness of the sample. This is an expected result, and gives rise to a relatively strong CD signal, which is positive for the left-handed and negative for the right-handed sample. For achiral cross samples there

should not be any CD signal. From the lower right corner of Figure 6.14, it can be seen that the CD response really is weaker and there is more variation for achiral than for the chiral samples, but some signal can still be observed.

However, we noticed that the intensity patterns, even within the identical measurement arrangements, are not totally comparable to each other between different measurements. For some reason, the sample is continuously drifting a bit on the sample plate, even in the time scale of our measurements, which is from tens of seconds to tens of minutes. This is why the CD calculations cannot be done without aligning the figures before. However, the alignment is challenging without any clear markers on the sample plate, and even if it would be possible, there are a few more issues. As was mentioned in Section 6.3, the sample particles are positioned too close to each other for distinguishing them clearly with our microscope, thus causing coupling between the particles. Furthermore, also sample burning under laser illumination affects the results. Hence, reliable CD analysis is impossible for these sample sets, and the calculated CD patterns in Figure 6.14 are only suggestive.

The THG intensity results measured from different samples with different polarizations are shown in Figure 6.15. The contrast between the excitation with RHCP and LHCP lights is here much weaker than what was achieved for SHG in Figure 6.14. Thus, the THG-CD figures are not shown, as the reliability of them would be even worse than for SHG. Instead, to try to compensate the effect of sample drift we determined an approximate CD analysis for different samples by picking some intensity values by hand and by using them for calculating the CD responses. Ten hot spots were chosen from each of the three sample sets and the intensity values for them were picked up from the figures measured with LHCP and RHCP light. Then, the averages of these peak values were calculated and the CD value of the sample was determined by using Eq. (2.49). The results are shown in Table 3. The same analysis was made also for SHG results introduced in Figure 6.14.

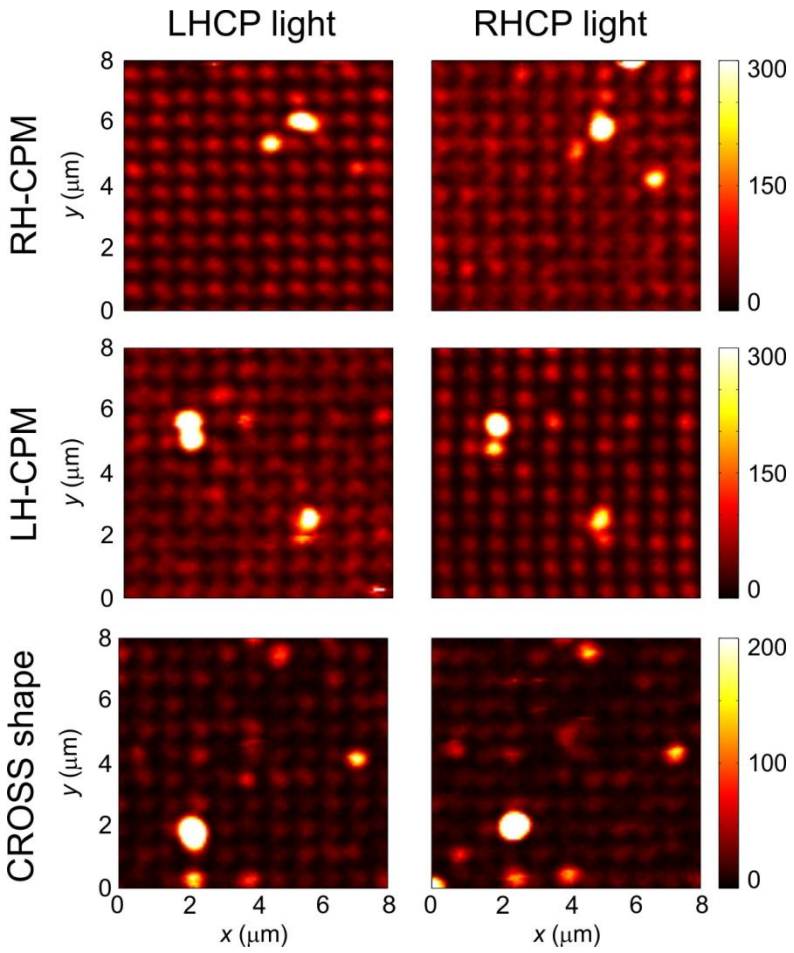

Figure 6.15. *THG intensity patterns of two chiral (RH- and LH-CPM) and one achiral (cross) sample when the excitation was made with LHCP and RHCP light.*

Table 3. *SHG- and THG-CD values for different samples calculated from 10 hot spots in intensity images.*

	SHG-CD	**THG-CD**
RH sample	-0.4906	0.0427
LH sample	0.8529	-0.1664
cross sample	0.2551	0.1657

Shown in Table 3 is a summary of the CD responses obtained from the nanoparticles. As expected, the SHG-CD values are strong and indicative of individual sample chirality. The non-zero SHG-CD values from the achiral samples suggest possible anisotropy, which was also evident in the SEM images (Figure 6.2). On the other hand, for these particles, THG-CD is a much weaker effect than SHG-CD. As the THG-CD responses are small and different for right- and left-handed samples, further studies should be done.

6.7 Spectral behaviour of nonlinear signals

The wide wavelength range of the used laser source enables, in principle, the implementation of spectral microscopy. In practise, however, the filters and detectors have relatively tight wavelength ranges, and for making wider spectral measurements they have to be changed accordingly during the measurement sequence. Thus, the spectral behaviour of SHG and THG and corresponding CD effects for the RH-CPM sample were here investigated by measuring the signals with only seven different excitation wavelengths between 1040 nm and 1070 nm. These measurements can be performed without making any modifications to the setup.

The total intensities of the SHG and THG intensity pattern images are shown in Figure 6.16a) as a function of the used excitation wavelength. It can be seen that the responses, both the SHG and THG, are strongest when the excitation wavelength is 1045 nm, and the signal decreases when the excitation wavelength is shorter or longer than that. The behaviour has the same character for SHG and THG and for both polarizations.

In principle, as the used detectors and filters are not changed when the wavelength is changed, the sensitivity of the measurement setup may be different for different wavelengths. However, the used wavelength range is relatively narrow and it should be inside the working ranges of the devices. Thus, the variation of the nonlinear signals along the spectrum is assumed to be because of the different natures of plasmon resonances of the particles. In the future, it would be interesting to investigate the spectral behaviour of the signals over a wider wavelength range.

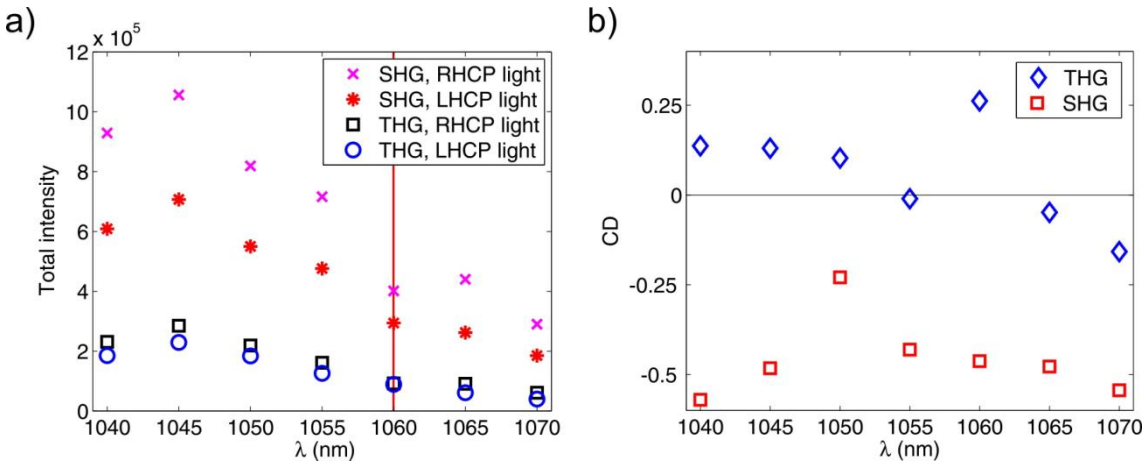

Figure 6.16. *a) Total intensities of SHG and THG intensity patterns measured from RH-CPM sample with different circular polarizations and different excitation wavelengths. The wavelength of 1060 nm, marked as a red line, is used in the other measurements shown in this Thesis. b) SHG- and THG-CD values for RH-CPM sample in function of excitation wavelength.*

As was already mentioned, the spectral behaviour is almost the same for signals excited with differently polarized incident beams. However, as can be seen from Figure

6.16a), there are some variations in the distance between the two SHG curves. This indicates that some spectral variation would probably be seen in the SHG-CD response, too. As expected based on the results introduces in the previous sections, the THG responses are almost the same with both polarizations.

The CD values were calculated for all used wavelengths from the intensity patterns (not shown), similarly than described in Section 6.6. The resulting graph is shown in Figure 6.16b). As expected, the absolute values of the THG-CD are smaller than the SHG-CD values, and some variation is seen along the spectrum. However, the changes are quite small and deeper analysis is not meaningful because of the origin of the responses is not totally sure and the calculation of the CD response is made only approximately.

7. CONCLUSION

In nonlinear optics, a powerful optical beam focused on a sample causes a response proportional to the higher powers of the excitation beam. This phenomenon can be applied, for example, to microscopy, where it is a general tool for investigating optical metamaterials and biological samples, to name a few. The benefits of the nonlinear techniques are, for instance, deeper penetration into tissue and higher contrast when compared to linear optical microscopy techniques. Furthermore, the nonlinear microscopy techniques are based on the natural properties of samples, meaning that no external labels are needed. Two widely used nonlinear microscopy techniques are based on second- (SHG) and third-harmonic (THG) generation. In SHG (THG), the wavelength of the signal is a half (one third) of the wavelength of the original excitation field. SHG and THG microscopies can be used, for instance, for investigating surface effects of nanoparticles and processes in biological systems. When the polarization of the excitation beam is varied, additional information about the sample structure can be gathered.

The main parts of a microscopy setup are the laser, appropriate polarizers, the focusing lens, the scanning stage and the detectors. The polarizers are used for changing the polarization of the excitation beam. The scanning stage is needed because the focused excitation beam illuminates only a small portion of the sample at a time. The main goal of this Thesis was to develop a user interface for a nonlinear microscope. This means that the control protocols for the polarizers, the scanning stage and the detectors had to be combined to a single program. Via this program, the user can define measurement settings, execute the measurements and save the results. The program was implemented with LabVIEW.

In our setup, a quarter-wave plate was used to control the polarization of the excitation beam, and two photomultiplier tubes were used as detectors, one for each measurement channel. The two channels were used for measuring the reflected SHG and THG signals, but another option would be, for example, to measure the reflected and transmitted SHG signals from a thin sample. The movement of the scanning stage was controlled by piezos and had a nanometer movement resolution. The integration of these devices to the user interface was done via the dynamic-link library files of these equipment and the whole program is based on the original control program of the nanopositioning stage, produced by the company Mad City Labs.

The operation of the program was tested with SHG and THG microscopy measurements on the three differently shaped plasmonic metamaterial samples. Two of the samples were designed to be chiral and one achiral. Chirality means that a particle or material has handedness, and it behaves differently under illumination with right- and left-

handed circular polarizations. This provides a possibility to implement circular dichroism (CD) microscopy measurements, where different absorption for light of different polarizations is utilized.

During the test measurements, the program was verified to work correctly and to be logical to use. The effects of different measurement parameters on the results were investigated and their behaviour was as expected. It is worth noticing, that the choice of the scan resolution and duration of signal collection at each pixel has to be set carefully. This is because the perfect option varies according to the measurement and sample type and, on the other hand, these parameters have a huge impact for the duration of the measurements.

Another fundamental test for the microscope was the verification of the detected signals and their behaviour when the power of the excitation beam was varied. The nonlinear signals were first verified using pulsed laser excitation. Furthermore, by using different kinds of filters to separate the various signals, it was confirmed that the detected signals really had the intended SHG and THG origins. Another proof for this was that the dependence of the SHG signal on the input power was quadratic, and that of the THG signal was cubic.

The SHG and THG measurements of the sample materials gave rise to the intensity patterns similar to the particle arrangements on the sample. However, the quality of the samples was not perfect and the particles were placed too close to each other for our purposes. Thus, the results we got are not totally reliable. We confirmed that all three samples have both SHG and THG responses and the SHG responses of the chiral samples were different for the two circular input polarizations, meaning that SHG-CD microscopy could be used to characterize these kinds of samples. However, for THG, the CD response was so low, that it is better not to make any conclusions about it. In the future, it will be interesting to study the origin of the CD effects more carefully and to find out whether THG-CD would also be a viable method. Furthermore, a wide spectral behaviour of the nonlinear CD signals would also be worthwhile to study.

All in all, the user interface developed in this Thesis seems to work properly, and can, in the future, be used for many kinds of nonlinear microscopy measurements. The interface is relatively easy to edit and new devices can be included in the program. The program is not restricted to SHG and THG microscopy only, but can be used, for instance, to nanolithography purposes. However, for microscopy measurements, the sample quality is a very important issue, as samples of poor quality cannot be measured with high reliability.

REFERENCES

[1] International Year of Light and Light Based Technologies, About the Year of Light, FAQ, website. Available (accessed on 3.2.2015): http://www.light2015.org/Home/About/FAQ.html

[2] Hecht E., Optics, 3rd ed., Addison Wesley Longman, Inc., USA, 1998, 694 p.

[3] Croft W.J., Under the Microscope: a Brief History of Microscopy, World Scientific, Singapore, 2006, 153 p.

[4] Franken P.A., Hill A.E., Peters C.W., Weinreich G., Generation of Optical Harmonics, Physical Review Letters, Vol. 7, Iss. 4, 1961, pp. 118–119.

[5] Carriles R., Schafer D.N., Sheetz K.E., Field J.J., Cisek R., Barzda V., Sylvester A.W., Squier J.A., Invited Review Article: Imaging Techniques for Harmonic and Multiphoton Absorption Fluorescence Microscopy, Review of Scientific Instruments, Vol. 80, Iss. 8, 2009, 081101.

[6] Débarre D., Supatto W., Pena A., Fabre A., Tordjmann T., Combettes L., Schanne-Klein M., Beaurepaire E., Imaging Lipid Bodies in Cells and Tissues Using Third-Harmonic Generation Microscopy, Nature Methods, Vol. 3, Iss. 1, 2006, pp. 47–53.

[7] Bautista G., Huttunen M.J., Kontio J.M., Simonen J., Kauranen M., Third- and Second-Harmonic Generation Microscopy of Individual Metal Nanocones Using Cylindrical Vector Beams, Optics Express, Vol. 21, Iss. 19, 2013, pp. 21918–21923.

[8] Klein M.V., Furtak T.E., Optics, 2nd ed., John Wiley & Sons, Inc., New York, USA, 1986, 660 p.

[9] Bennett C.A., Principles of Physical Optics, 1st ed., John Wiley & Sons, Inc., Hoboken, USA, 2008, 492 p.

[10] Boyd R.W., Nonlinear Optics, 3rd ed., Elsevier Science, USA, 2008, 635 p.

[11] Yariv A., Yeh P., Optical Waves in Crystals, Propagation and Control of Laser Radiation, Wiley Classics Library Edition, John Wiley & Sons, Inc., Hoboken, USA, 2003, 589 p.

[12] Tipler P.A., Llewellyn R.A., Modern Physics, 4th ed., W.H. Freeman and Company, New York, USA, 2004, 669 p.

[13] Naskali L., Huttunen M.J., Virkki M., Bautista G., Dér A., Kauranen M., Microscopic Determination of Second-Order Nonlinear Optical Susceptibility Tensors, The Journal of Physical Chemistry C, Vol. 118, Iss. 45, 2014, pp. 26409–26414.

[14] Huttunen M.J., Partanen M., Bautista G., Chu S.-W., Kauranen M., Nonlinear Optical Activity Effects in Complex Anisotropic Three-Dimensional Media, Optical Materials Express, Vol. 5, Iss.1, 2015, pp. 11–21.

[15] Saleh B.E.A., Teich M.C., Fundamentals of Photonics, 2nd ed., John Wiley & Sons, Inc., Hoboken, USA, 2007, 1177 p.

[16] Brasselet S., Polarization-Resolved Nonlinear Microscopy: Application to Structural Molecular and Biological Imaging, Advances in Optics and Photonics, Vol. 3, Iss. 3, 2011, pp. 205–271.

[17] Zumdahl S.S., Chemical Principles, 6th ed., Houghton Mifflin Company, Boston, USA, 2009, 1073 p.

[18] Brown T.L., LeMay H.E. Jr., Bursten B.E., Murphy C.J., Woodward P.M., Chemistry The Central Science, 12th ed., International Edition, Pearson Education, Inc., Boston, USA, 2012, 1050 p.

[19] Leidler K.J., Meiser J.H., Sanctuary B.C., Physical Chemistry, 4th ed., Houghton Mifflin Company, Boston, USA, 2003, 998 p.

[20] Prasad P.N., Introduction to Biophotonics, 1st ed., John Wiley & Sons, Inc., Hoboken, USA, 2003, 593 p.

[21] Wagnière G., Optical Activity of Higher Order in a Medium of Randomly Oriented Molecules, The Journal of Chemical Physics, Vol. 77, Iss. 6, 1982, pp. 2786–2792.

[22] Nunes J.A., Tong W.G., Sensitive Circular Dichroism Spectroscopy Based on Nonlinear Degenerate Four-Wave Mixing, Analytical Chemistry, Vol. 65, Iss. 21, 1993, pp. 2990–2994.

[23] Petralli-Mallow T., Wong T.M., Byers J.D., Yee H.I., Hicks J.M., Circular Dichroism Spectroscopy at Interfaces: A Surface Second Harmonic Generation Study, The Journal of Physical Chemistry, Vol. 97, Iss. 7, 1993, pp. 1383–1388.

[24] Verbiest T., Kauranen M., Persoons A., Ikonen M., Kurkela J., Lemmetyinen H., Nonlinear Optical Activity and Biomolecular Chirality, Journal of the American Chemical Society, Vol. 116, Iss. 20, 1994, pp. 9203–9205.

[25] Lee H., Huttunen M.J., Hsu K.-J., Partanen M., Zhuo G.-Y., Kauranen M., Chu S.-W, Chiral Imaging of Collagen by Second-Harmonic Generation Circular Dichroism, Biomedical Optics Express, Vol. 4, Iss. 6, 2013, pp. 909–916.

[26] Bautista G., Pfisterer S., Huttunen M., Ranjan S., Kanerva K., Ikonen E., Kauranen M., Polarized THG Microscopy Identifies Compositionally Different Lipid Droplets in Mammalian Cells, Biophysical Journal, Vol. 107, Iss. 10, 2014, pp. 2230–2236.

[27] Träger F. (ed.), Springer Handbook of Lasers and Optics, 2nd ed., Springer, Berlin, Germany, 2012, 1694 p.

[28] Diaspro A. (ed.), Optical Fluorescence Microscopy: From the Spectral to the Nano Dimension, 1st ed., Springer, Berlin, Germany, 2011, 244 p.

[29] Helmchen F., Denk W., Deep Tissue Two-Photon Microscopy, Nature Methods, Vol. 2, Iss. 12, 2005, pp. 932–940.

[30] Di Bartolo B., Collins J. (eds.), Biophotonics: Spectroscopy, Imaging, Sensing and Manipulation, Springer, Dordrecht, The Netherlands, 2009, 400 p.

[31] Mertz J., Nonlinear Microscopy: New Techniques and Applications, Current Opinion in Neurobiology, Vol. 14, Iss. 5, 2004, pp. 610–616.

[32] Campagnola P., Second Harmonic Generation Imaging Microscopy: Applications to Diseases Diagnostics, Analytical Chemistry, Vol. 83, Iss. 9, 2011, pp. 3224–3231.

[33] Huttunen M.J., Bautista G., Decker M., Linden S., Wegener M., Kauranen M., Nonlinear Chiral Imaging of Subwavelength-Sized Twisted-Cross Gold Nanodimers [Invited], Optical Materials Express, Vol. 1, Iss. 1, 2011, pp. 46–56.

[34] Bautista G., Huttunen M.J., Mäkitalo J., Kontio J.M., Simonen J., Kauranen M., Second-Harmonic Generation Imaging of Metal Nano-Objects with Cylindrical Vector Beams, Nano Letters, Vol. 12, Iss. 6, 2012, pp. 3207–3212.

[35] Huttunen M.J., Herranen O., Johansson A., Jiang H., Mudimela P.R., Myllyperkiö P., Bautista G., Nasibulin A.G., Kauppinen E.I., Ahlskog M., Kauranen M., Pettersson M., Measurement of Optical Second-Harmonic Generation from an Individual Single-Walled Carbon Nanotube, New Journal of Physics, Vol. 15, 2013, 083043.

[36] Kim H., Sheps T., Collins P.G., Potma E.O., Nonlinear Optical Imaging of Individual Carbon Nanotubes with Four-Wave-Mixing Microscopy, Nano Letters, Vol. 9, Iss. 8, 2009, pp. 2991–2995.

[37] Kauranen M., Zayats A.V., Nonlinear Plasmonics, Nature Photonics, Vol. 6, Iss. 11, 2012, pp. 737–748.

[38] Oheim M., Michael D.J., Geisbauer M., Madsen D., Chow R.H., Principles of Two-Photon Excitation Fluorescence Microscopy and Other Nonlinear Imaging Approaches, Advanced Drug Delivery Reviews, Vol. 58, Iss. 7, 2006, pp. 788–808.

[39] Zipfel W.R., Williams R.M., Webb W.W., Nonlinear Magic: Multiphoton Microscopy in the Biosciences, Nature Biotechnology, Vol. 21, Iss. 11, 2003, pp. 1369–1377.

[40] Chen W.S., Wang Y., Liu N.R., Zhang J.X., Chen R., Multiphoton Microscopic Imaging of Human Normal and Cancerous Oesophagus Tissue, Journal of Microscopy, Vol. 253, Iss. 1, 2014, pp. 79–82.

[41] Yu C.-H., Tai S.-P., Kung C.-T., Wang I.-J., Yu H.-C., Huang H.-J., Lee W.-J., Chan Y.-F., Sun C.-K., In Vivo and Ex Vivo Imaging of Intra-Tissue Elastic Fibers Using Third-Harmonic-Generation Microscopy, Optics Express, Vol. 15, Iss. 18, 2007, pp. 11167–11177.

[42] Chen X., Raggio C., Campagnola P.J., Second-Harmonic Generation Circular Dichroism Studies of Osteogenesis Imperfecta, Optics Letters, Vol. 37, Iss. 18, 2012, pp. 3837–3839.

[43] Zhuo G.-Y., Lee H., Hsu K.-J., Huttunen M.J., Kauranen M., Lin Y.-Y., Chu S.-W., Three-Dimensional Structural Imaging of Starch Granules by Second-Harmonic Generation Circular Dichroism, Journal of Microscopy, Vol. 253, Iss. 3, 2014, pp. 183–190.

[44] Cai W., Shalaev V., Optical Metamaterials: Fundamentals and Applications, 1st ed., Springer, New York, USA, 2010, 200 p.

[45] Prasad P.N., Nanophotonics, 1st ed., John Wiley & Sons, Inc., Hoboken, USA, 2004, 415 p.

[46] Czaplicki R., Husu H., Siikanen R., Mäkitalo J., Kauranen M., Laukkanen J., Lehtolahti J., Kuittinen M., Enhancement of Second-Harmonic Generation from Metal Nanoparticles by Passive Elements, Physical Review Letters, Vol. 110, Iss. 9, 2013, 093902.

[47] Murugkar S., De Leon I., Horton M., Qassim H., Leach J., Boyd R.W., Planar Chiral Metamaterials for Biosensing Applications, Progress in Biomedical Optics and Imaging - Proceedings of SPIE, Vol. 8597, 2013.

[48] Gauderon R., Lukins P.B., Sheppard C.J., Optimization of Second-Harmonic Generation Microscopy, Micron, Vol. 32, Iss. 7, 2001, pp. 691–700.

[49] Shung K.K., Diagnostic Ultrasound - Imaging Blood Flow Measurements, 1st ed., CRC Press, Taylor & Francis Group, Boca Raton, USA, 2005, 232 p.

[50] PMS-300, PMS-400 and PMS-400A, 800 MHz Gated Photon Counters/Multiscalers, Operator's Manual, Becker & Hickl GmbH, Berlin, Germany, 2004, 72 p.

[51] Hamamatsu Photonics K.K. Editorial Committee (ed.), Photomultiplier Tubes Basics and Applications, 3rd ed., Hamamatsu Photonics K.K. Electron Tube Division, 2006, 309 p.

[52] De Leon I., Department of Physics and School of Electrical Engineering and Computer Science, University of Ottawa, Ottawa, Canada ON K1N 6N5. Personal Communication.

APPENDIX 1: SPECIFICATIONS OF SPECTRAL FILTERS

Filter	Edge/central wavelength (nm)	Wavelength range for transmission (nm)	Used for
FF409-Di03-25x36	409	415-950	first filter at SHG arm
FI01-531/22-25	531	520-542	second filter at SHG arm
Infrared block		<900 nm	first filter at THG arm
FI01-355/40-25	355	335-375	second filter at THG arm
FI01-340/12-25	340	334-346	verification of THG signal
FI01-376/20-25	376	366-386	verification of THG signal
FI01-470/28-25	470	456-484	verification of SHG signal
FI01-580/14-25	580	573-587	verification of SHG signal
FI01-629/56-25	629	601-657	verification of SHG signal

APPENDIX 2: FRONT PANEL OF THE USER INTERFACE

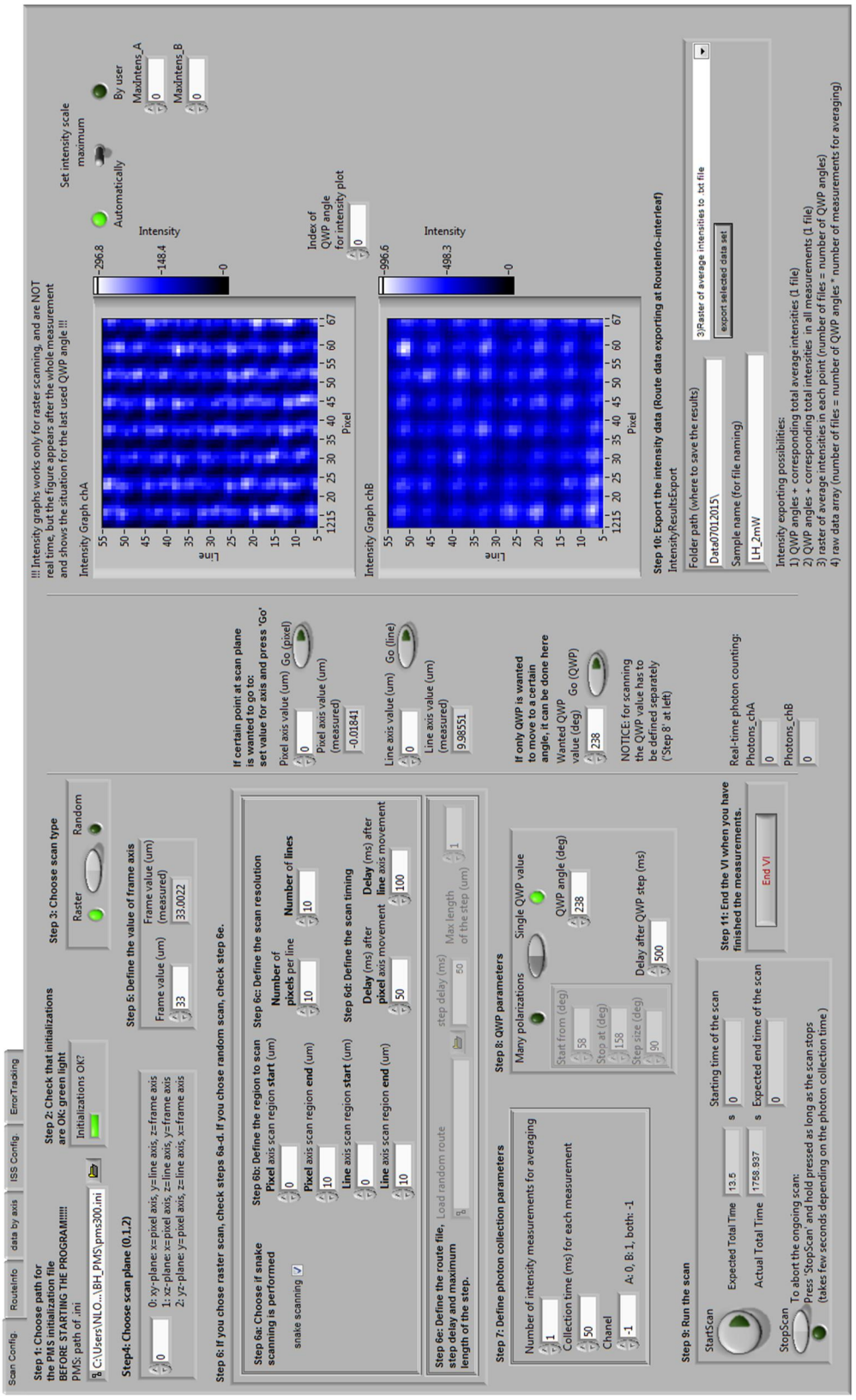

Option	Info text	Results (and number of files)
Raw data	Intensity in the n. measurement round at each measurement location. Each n measurement occasions has their own file. On the other hand: 1st value in a file: Intensity in the 1st measurement location. 2nd value: Intensity in 2nd measurement location. etc. Each used QWP angle has its own files. Actual measured QWP values (deg): 238.000000 328.001000	2.000 1.000 1.000 1.000 1.000 0.000 1.000 0.000 1.000 Number of result files for each channel: 6 (because of 2 QWP angles and 3 measurement for averaging)
Intensity raster	Values are the average intensities in each measurement location so that element (1,1) corresponds to raster point (line_1,pixel_1) and element (n,m) corresponds to raster point (line_n,pixel_m). Each used QWP angle has its own file. Actual measured QWP values (deg): 238.000000 328.001000	2.000 1.667 1.000 0.667 0.667 0.333 1.667 0.667 1.333 Number of result files for each channel: 2 (because of 2 QWP angles)
Total intensities	1. column: QWP angles (deg) 2. column: total intensity (over the scan area) in 1. measurement round 3. column: total intensity (over the scan area) in 2. measurement round n. column: total intensity (over the scan area) in (n-1)th measurement round	238.000 8.000 12.000 10.000 328.001 15.000 14.000 12.000 Number of result files for each channel: 1
Total average intensities	1. column: QWP angles (deg) 2. column: total intensity (average over all measurement rounds)	238.000 10.000 328.001 13.667 Number of result files for each channel: 1